Cancer Cell

Article

KMT2D Deficiency Impairs Super-Enhancers to Confer a Glycolytic Vulnerability in Lung Cancer

Graphical Abstract

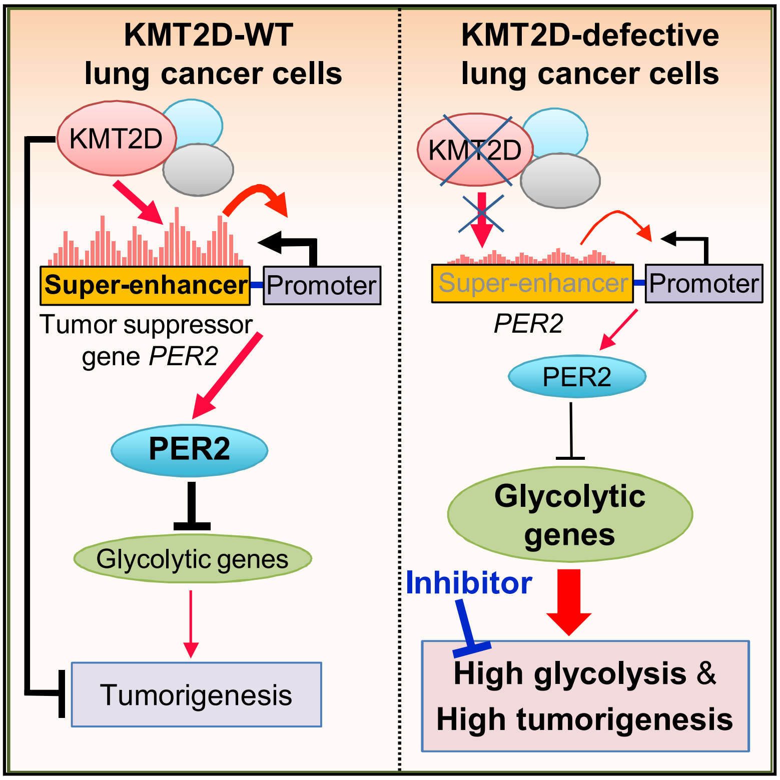

Highlights

- Lung-specific *Kmt2d* loss in mice promotes lung tumorigenesis
- *Kmt2d* loss impairs enhancers, including a super-enhancer for the tumor suppressor *Per2*
- KMT2D activates *Per2* expression and thereby represses glycolytic genes
- Glycolysis inhibition impedes the growth of KMT2D-mutant lung cancer

Authors

Hunain Alam, Ming Tang,
Mayinuer Maitituoheti, ...,
Laura Baseler, Kunal Rai, Min Gyu Lee

Correspondence

KRai@mdanderson.org (K.R.),
mglee@mdanderson.org (M.G.L.)

In Brief

Histone methyltransferase KMT2D is frequently mutated in lung tumors, and Alam et al. identify KMT2D as a lung tumor suppressor. KMT2D deficiency induces aberrant metabolic reprogramming via super-enhancer impairment, conferring sensitivity to glycolytic inhibitors in lung cancer with KMT2D-inactivating mutations.

Alam et al., 2020, Cancer Cell *37*, 1–19
April 13, 2020 © 2020 Elsevier Inc.
https://doi.org/10.1016/j.ccell.2020.03.005

Please cite this article in press as: Alam et al., KMT2D Deficiency Impairs Super-Enhancers to Confer a Glycolytic Vulnerability in Lung Cancer, Cancer Cell (2020), https://doi.org/10.1016/j.ccell.2020.03.005

Cancer Cell
Article

CellPress

KMT2D Deficiency Impairs Super-Enhancers to Confer a Glycolytic Vulnerability in Lung Cancer

Hunain Alam,[1,10] Ming Tang,[2,10] Mayinuer Maitituoheti,[2] Shilpa S. Dhar,[1] Manish Kumar,[1] Chae Young Han,[1] Chandrashekar R. Ambati,[3] Samir B. Amin,[2] Bingnan Gu,[1] Tsai-Yu Chen,[1] Yu-Hsi Lin,[4] Jichao Chen,[5] Florian L. Muller,[4] Nagireddy Putluri,[3] Elsa R. Flores,[6] Francesco J. DeMayo,[7] Laura Baseler,[8,9] Kunal Rai,[2,*] and Min Gyu Lee[1,11,*]
[1]Department of Molecular & Cellular Oncology, The University of Texas MD Anderson Cancer Center, 1515 Holcombe Boulevard, Houston, TX 77030, USA
[2]Department of Genomic Medicine, The University of Texas MD Anderson Cancer Center, 1901 East Road, Houston, TX 77054, USA
[3]Advanced Technology Core and Department of Molecular and Cell Biology, Baylor College of Medicine, Houston, TX 77030, USA
[4]Department of Cancer Systems Imaging, The University of Texas MD Anderson Cancer Center, 1881 East Road, Houston, TX 77054, USA
[5]Department of Pulmonary Medicine, The University of Texas MD Anderson Cancer Center, Houston, TX 77030, USA
[6]Department of Molecular Oncology and Cancer Biology and Evolution Program, Moffitt Cancer Center, 12902 Magnolia Drive, Tampa, FL 33612, USA
[7]Reproductive and Developmental Biology Laboratory, The National Institute of Environmental Health Sciences, 111 T.W. Alexander Drive, Research Triangle Park, NC 27709, USA
[8]Department of Veterinary Medicine & Surgery, The University of Texas MD Anderson Cancer Center, 1515 Holcombe Boulevard, Houston, TX 77030, USA
[9]Present address: NAMSA, 6750 Wales Road, Northwood, OH 43619, USA
[10]These authors contributed equally
[11]Lead Contact
*Correspondence: KRai@mdanderson.org (K.R.), mglee@mdanderson.org (M.G.L.)
https://doi.org/10.1016/j.ccell.2020.03.005

SUMMARY

Epigenetic modifiers frequently harbor loss-of-function mutations in lung cancer, but their tumor-suppressive roles are poorly characterized. Histone methyltransferase KMT2D (a COMPASS-like enzyme, also called MLL4) is among the most highly inactivated epigenetic modifiers in lung cancer. Here, we show that lung-specific loss of *Kmt2d* promotes lung tumorigenesis in mice and upregulates pro-tumorigenic programs, including glycolysis. Pharmacological inhibition of glycolysis preferentially impedes tumorigenicity of human lung cancer cells bearing KMT2D-inactivating mutations. Mechanistically, *Kmt2d* loss widely impairs epigenomic signals for super-enhancers/enhancers, including the super-enhancer for the circadian rhythm repressor *Per2*. Loss of *Kmt2d* decreases expression of PER2, which regulates multiple glycolytic genes. These findings indicate that KMT2D is a lung tumor suppressor and that KMT2D deficiency confers a therapeutic vulnerability to glycolytic inhibitors.

INTRODUCTION

Lung cancer accounts for more cancer deaths than any other type of cancer among both men and women. The overall 5-year survival rate for lung cancer is low (~18.1%). Lung cancer is often characterized by gain-of-function mutations and amplification of oncogenic kinase genes (e.g., *KRAS* and *EGFR*) as well as loss-of-function alterations in tumor-suppressor genes (e.g., *TP53* and *LKB1*) (Cancer Genome Atlas Research Network, 2014; Herbst et al., 2008; Imielinski et al., 2012). Much research for

Significance

Lung cancer is the leading cause of cancer deaths. The overall survival rate for patients with lung cancer remains low despite recent therapeutic advances, and a majority of lung cancer patients lack a druggable target. Therefore, there is a great need for a better understanding of the molecular mechanisms driving lung cancer. Epigenetic modifiers are frequently lost in lung cancer, but how this provokes lung tumorigenesis remains unclear. We show that KMT2D, which is recurrently mutated in lung cancer, is a lung tumor suppressor. Our results uncover a tumor-promoting epigenetic mechanism by which KMT2D-inactivating mutations induce aberrant metabolic reprogramming via super-enhancer impairment in lung cancer. Our findings support a glycolysis-inhibitory approach as a therapeutic intervention strategy against *KMT2D*-mutant lung cancer.

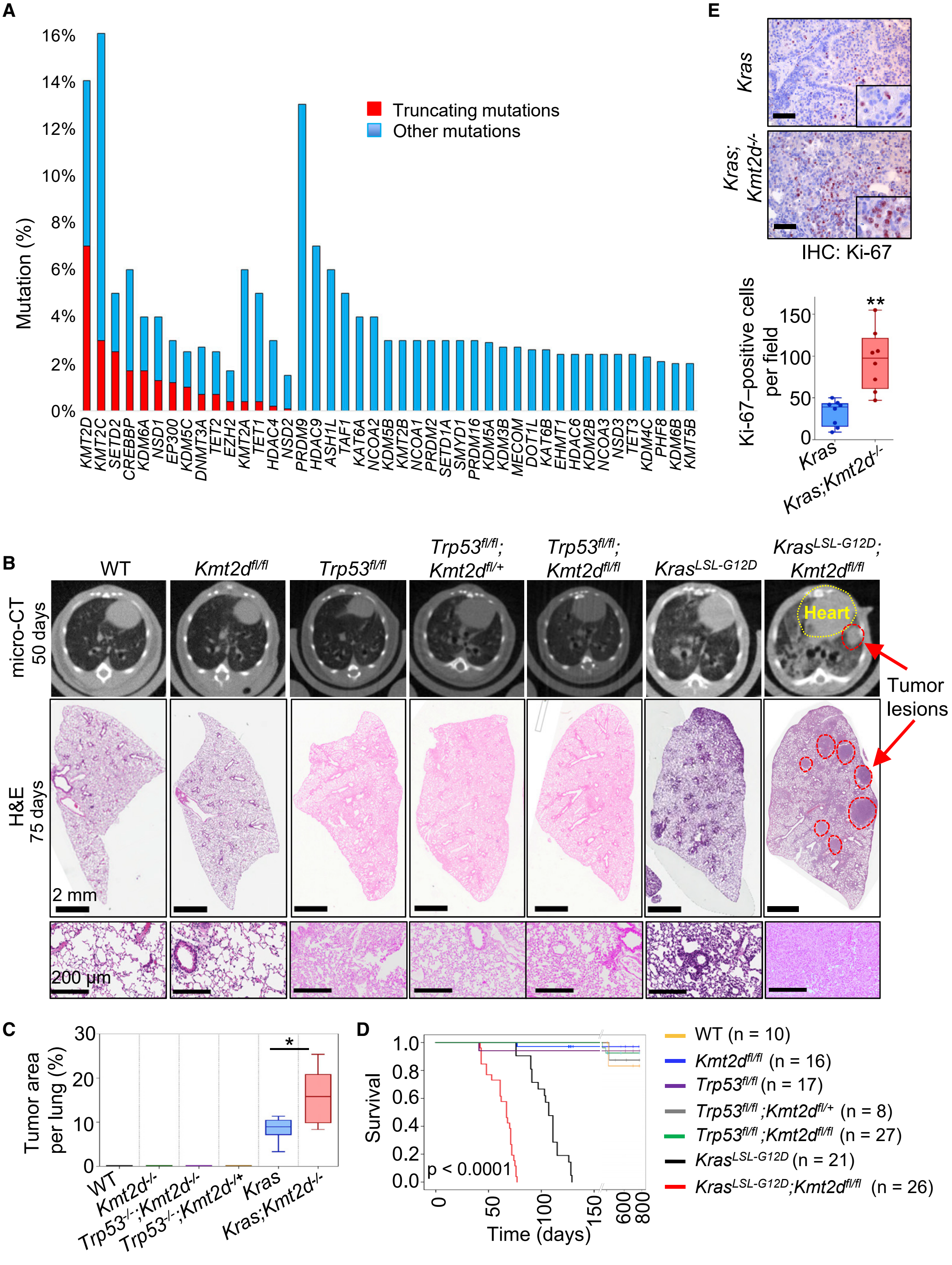

(legend on next page)

lung cancer has focused on kinase signaling pathways, leading to the development of the kinase-targeted therapies such as the EGFR (epidermal growth factor receptor) mutant inhibitors and the ALK (anaplastic lymphoma kinase) inhibitors. However, a vast majority of lung cancer patients who are treated with the kinase-targeted therapies later experience tumor relapse and drug resistance (Herbst et al., 2008; Sharma et al., 2007). Recently, the use of immune checkpoint inhibitors (e.g., anti-PD1 and anti-PD-L1) has provided significant survival benefit for patients with lung cancer whose lung tumor expresses a high level of PD-L1. However, the prognosis for many lung cancer patients remains poor (Herbst et al., 2018; Malhotra et al., 2017). Moreover, a majority of these patients do not have a well-defined drug target (Chan and Hughes, 2015; Herbst et al., 2018). For these reasons, there is a great need for further mechanistic understanding of lung cancer to be used for more effective therapeutic approaches for the treatment of lung cancer.

Epigenetic alterations, which represent heritable aberrations in gene expression or cellular phenotype without alterations of DNA sequences, have emerged as a major type of cancer-driving events (Dawson and Kouzarides, 2012). Covalent modifications of DNA and histones play a key role in epigenetic regulation of gene expression and include DNA methylation, histone acetylation, and histone methylation. Interestingly, histone methylation, which can occur at lysine and arginine residues in histones, is linked to either gene activation or silencing, depending on the methylation residues within the histones (Barski et al., 2007). Notably, histone methylation modifiers and other epigenetic modifiers are often mutated in lung tumors, including lung adenocarcinoma (LUAD) and lung squamous cell carcinoma (LUSC), which comprise 40%–50% and 25%–30% of lung cancer, respectively (Campbell et al., 2016; Cancer Genome Atlas Research Network, 2012, 2014; Imielinski et al., 2012; Kandoth et al., 2013). In fact, a substantial percentage of such mutations results in loss of function, suggesting that epigenetic modifiers can have tumor-suppressive functions. However, their tumor-suppressive roles in lung cancer remain to be established. In the present study, we sought to identify an epigenetic modifier with tumor-suppressive function in lung cancer.

RESULTS

Lung-Specific Loss of *Kmt2d* Strongly Promotes $\text{KRAS}^{\text{G12D}}$-Induced LUAD in Mice

To identify an epigenetic modifier with tumor-suppressive function in lung cancer, we examined which epigenetic modifiers most frequently undergo genomic alterations (i.e., truncations, missense mutations, and insertions/deletions) that are related to loss-of-function mutations in lung tumors. Our analysis of pan-lung cancer data (LUAD and LUSC) in The Cancer Genome Atlas (TCGA) database showed that the gene encoding the histone methyltransferase KMT2D (a COMPASS-like enzyme, also called MLL4, MLL2, and ALR) (Shilatifard, 2012) harbored such genomic alterations in about 14% of lung tumor samples (Figures 1A and S1A). Of the genomic alterations in *KMT2D*, 48.7% were truncating mutations, which was the highest percentage of all the epigenetic modifiers examined. A vast majority of the KMT2D truncations cause loss of function because the catalytic SET domain (amino acids 5,397–5,513) is located at the C terminus of KMT2D and loss of a large portion of the SET would destabilize KMT2D protein (Dorighi et al., 2017; Jang et al., 2019). Thus, our analysis indicates that KMT2D is among the most highly inactivated epigenetic modifiers (Figure 1A). Interestingly, *KMT2D* was mutated in substantial portions of both LUAD (e.g., ~7.8%) and LUSC (e.g., ~22.4%) samples (Figures S1B and S1C). Of note, it has been reported that a majority of *KMT2D* missense mutations in lymphoma significantly reduce KMT2D enzymatic activity, indicating a negative effect of *KMT2D* missense mutations on KMT2D activity (Zhang et al., 2015a). Because these findings indicate that KMT2D is a candidate lung tumor suppressor with frequent genomic alterations, we chose to characterize the role of KMT2D in lung cancer in subsequent analyses.

We analyzed whether *KMT2D* alterations frequently co-occur with alterations in the two most frequently mutated genes *TP53* and *KRAS* in human lung cancer. About 71% of *KMT2D* alterations co-occur with *TP53* alterations in lung tumors, and about 22% of *KMT2D* alterations coincide with *KRAS* alterations in LUAD (Figure S1D). Therefore, we sought to determine whether lung-specific loss of *Kmt2d* cooperates with *Trp53* inactivation or *Kras* activation for lung tumorigenesis in mice. We first generated several genetically engineered mouse models (GEMMs), including $Trp53^{fl/fl}$;$Kmt2d^{fl/fl}$ and $Kras^{LSL\text{-}G12D}$;$Kmt2d^{fl/fl}$ (Figures S2A–S2C). We then induced Cre-mediated deletion of *loxP* sites by infecting the lungs of 6- to 10-week-old GEMM mice with Adeno-Cre viruses via the intratracheal intubation method (DuPage et al., 2009) and monitored their lungs at 6- to 8-week intervals for up to 125 days post infection by performing micro-computed tomography (micro-CT) scans. Lung-specific single loss or co-loss of *Kmt2d* and *Trp53* by Adeno-Cre-mediated deletion neither induced any detectable tumor in mouse lungs for up to 16 months post infection nor changed mouse survival times (Figures 1B–1D

Figure 1. The Loss of *Kmt2d*, Whose Human Homolog Is among the Most Highly Mutated Epigenetic Modifiers in Lung Cancer, Strongly Accelerates KRAS-driven LUAD in Mice

(A) Comparison of gene alterations of epigenetic modifiers (histone acetyltransferases and deacetylases, histone methyltransferases and demethylases, and DNA modifiers) in the TCGA Pan-lung cancer dataset. Other mutations represent missense and inframe mutations.

(B) Representative images of micro-CT scans (top panels) and H&E-stained tissues (middle and bottom panels) of wild-type (WT), $Kmt2d^{fl/fl}$, $Trp53^{fl/fl}$, $Trp53^{fl/fl}$;$Kmt2d^{fl/+}$, $Trp53^{fl/fl}$;$Kmt2d^{fl/fl}$, $Kras^{LSL\text{-}G12D}$, and $Kras^{LSL\text{-}G12D}$;$Kmt2d^{fl/fl}$ mice. The lungs of the mice were infected with Adeno5 (Ad5)-CMV-Cre viruses.

(C) Comparison of tumor area (%) per mouse in the indicated groups of mice (n = 6).

(D) Kaplan-Meier survival analysis of the indicated groups of mice. Statistical analysis was performed using the two-sided log-rank test.

(E) Immunohistochemistry (IHC) analysis for the cell proliferation marker Ki-67 in *Kras* and *Kras*;$Kmt2d^{-/-}$ lung tumors. Ki-67-positive cells in ten random fields of three different tumors each from *Kras* and *Kras*;$Kmt2d^{-/-}$ groups were quantified. Scale bars represent 50 μm.

In the box plots in (C) and (E), the bottom and the top rectangles indicate the first quartile (Q1) and third quartile (Q3), respectively. The horizontal lines in the middle signify the median (Q2), and the vertical lines that extend from the top and the bottom of the plot indicate the maximum and minimum values, respectively. $^{*}p < 0.05$, $^{**}p < 0.01$ (two-tailed Student's t test). See also Figures S1 and S2.

Please cite this article in press as: Alam et al., KMT2D Deficiency Impairs Super-Enhancers to Confer a Glycolytic Vulnerability in Lung Cancer, Cancer Cell (2020), https://doi.org/10.1016/j.ccell.2020.03.005

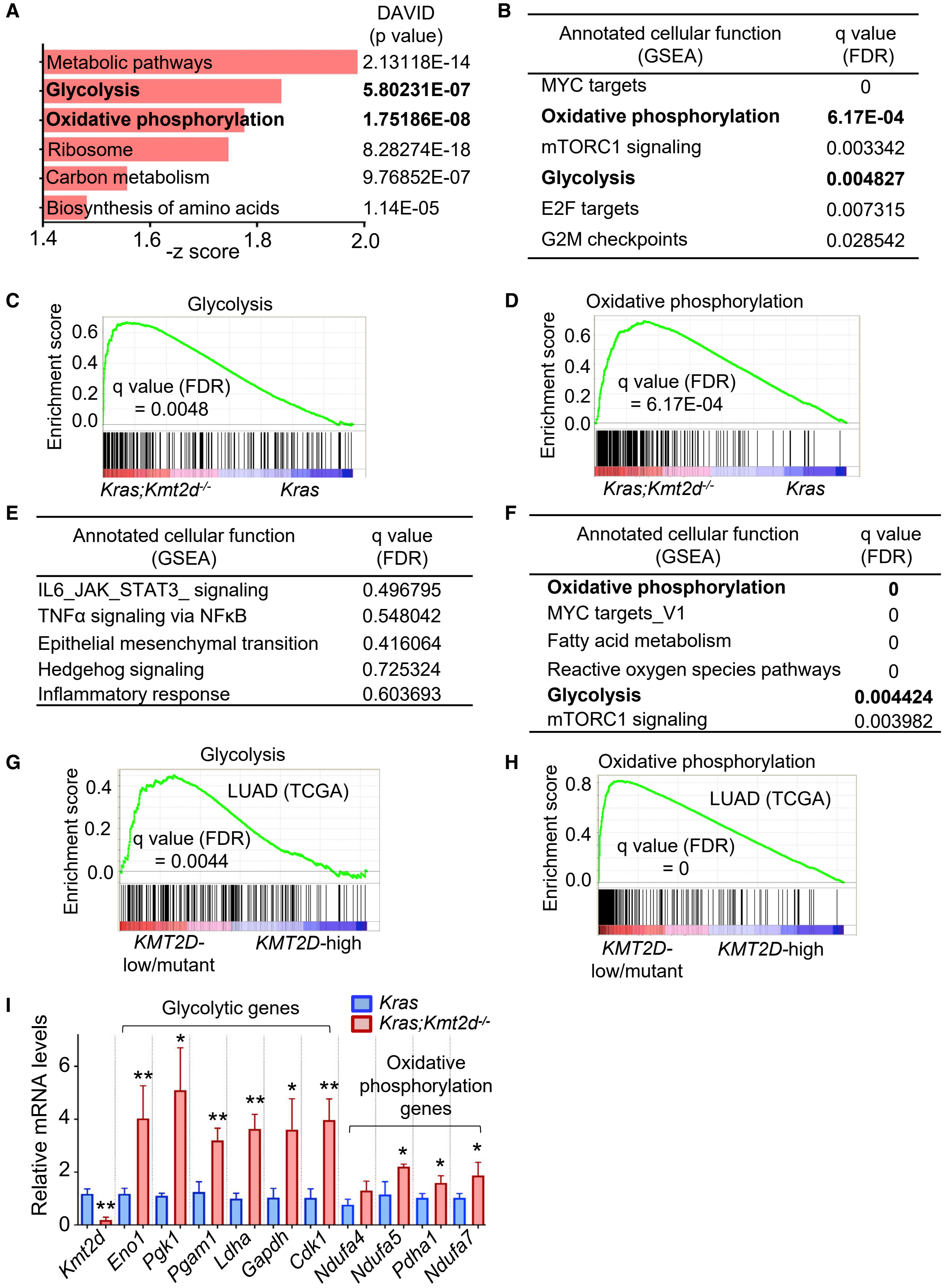

B

Annotated cellular function (GSEA)	q value (FDR)
MYC targets	0
Oxidative phosphorylation	**6.17E-04**
mTORC1 signaling	0.003342
Glycolysis	**0.004827**
E2F targets	0.007315
G2M checkpoints	0.028542

E

Annotated cellular function (GSEA)	q value (FDR)
IL6_JAK_STAT3_ signaling	0.496795
TNFα signaling via NFκB	0.548042
Epithelial mesenchymal transition	0.416064
Hedgehog signaling	0.725324
Inflammatory response	0.603693

F

Annotated cellular function (GSEA)	q value (FDR)
Oxidative phosphorylation	**0**
MYC targets_V1	0
Fatty acid metabolism	0
Reactive oxygen species pathways	0
Glycolysis	**0.004424**
mTORC1 signaling	0.003982

Figure 2. *Kmt2d* Loss Upregulates Tumor-Promoting Programs, Such as Glycolysis

(A) Ontology analysis of genes ($n = 1,113$, $p < 0.05$) upregulated by *Kmt2d* loss in KRAS-driven mouse LUAD. Gene expression profiles were compared between *Kras* tumors and *Kras;Kmt2d*$^{-/-}$ tumors. The functional annotation tool DAVID was used for the analysis. Metabolic pathways include genes for glycolysis, oxidative phosphorylation (OXPHOS), and tricarboxylic acid cycle.

(legend continued on next page)

and S2D). This may be partly because *Trp53* loss alone rarely induces lung tumors in mice, although *Trp53* loss promotes oncogene-driven lung tumorigenesis (Donehower et al., 1992; DuPage et al., 2009; Lang et al., 2004; Olive et al., 2004). In addition, because KMT2D and p53 in a multi-protein complex may activate a similar set of the DNA-damage response pathway genes (Lee et al., 2009), their co-loss may not cooperate for tumorigenesis. For KRAS-induced lung tumorigenesis, we used a $Kras^{LSL\text{-}G12D}$ model (hereafter referred to as the *Kras* model) because it is a well-established GEMM for LUAD (DuPage et al., 2009). *Kras* activation was induced by lung-specific deletion of the LSL (loxP-STOP-loxP) cassette via Adeno-Cre virus infection, as previously described (Jackson et al., 2001). To examine whether *Kmt2d* loss promotes KRAS-induced lung tumorigenesis, we monitored tumor formation in *Kras* and *Kras*;$Kmt2d^{fl/fl}$ lungs, as described above.

Data from micro-CT scans and hematoxylin and eosin (H&E)-stained tumor sections showed that lung-specific loss of *Kmt2d* promoted KRAS-induced lung tumorigenesis (Figures 1B and 1C). Specifically, our H&E data demonstrated that a higher percentage of the pulmonary parenchyma was effaced by tumors in the *Kras*;$Kmt2d^{-/-}$ group of mice than in the *Kras* group of mice (Figures 1B, 1C, S2E, and S2F). Consistent with the enhancement of tumorigenicity by *Kmt2d* loss, immunohistochemistry (IHC) analysis showed that levels of the cell proliferation marker Ki-67 were increased by *Kmt2d* loss (Figure 1E). Like *Kras* lung tumors, *Kras*;$Kmt2d^{-/-}$ lung tumors were positive for the well-known LUAD marker TTF-1 (alias NKX2.1) and weak for expression of Keratin 5 (an LUSC marker), indicating their LUAD characteristics (Figure S2G). Our survival analysis demonstrated that *Kmt2d* loss significantly shortened the survival of mice bearing *Kras* pulmonary tumors (Figure 1D) and that low *KMT2D* mRNA levels were associated with poor prognosis in LUAD but not LUSC patients (Figures S2H and S2I). These results, along with those aforementioned, suggest that *Kmt2d* loss, like *Trp53* loss, promotes rather than initiates LUAD tumorigenesis.

Glycolysis Program Upregulated by *Kmt2d* Loss Has Human LUAD Relevance

To understand how lung-specific loss of *Kmt2d* promotes LUAD, we isolated tumor lesions from *Kras* and *Kras*;$Kmt2d^{-/-}$ lungs and compared their gene expression profiles using RNA sequencing (RNA-seq). Our RNA-seq data confirmed Cre-mediated deletion of *loxP* in *Kmt2d*, as RNA peaks corresponding to exons 16–19 of *Kmt2d* were greatly reduced (Figure S2J). Bioinformatics analyses of RNA-seq data using DAVID tools and gene set enrichment analysis (GSEA) both showed that genes for glycolysis and oxidative phosphorylation (OXPHOS) pathways were upregulated by *Kmt2d* loss (Figures 2A–2D and Table S1). In contrast, these two analyses did not share a pathway downregulated by *Kmt2d* loss, as GSEA analysis did not show any pathway that was significantly downregulated by *Kmt2d* loss (Figure 2E). In line with our RNA-seq results, analysis of TCGA lung cancer database showed that glycolytic and OXPHOS genes were enriched in human *KMT2D*-low/mutant LUAD samples compared with human *KMT2D*-high LUAD samples (Figures 2F–2H and Table S2). Robust upregulation of glycolytic genes *Eno1*, *Pgk1*, *Pgam1*, *Ldha*, *Gapdh*, and *Cdk1* by *Kmt2d* loss was confirmed by quantitative RT-PCR (qRT-PCR) (Figure 2I). In contrast, most genes for OXPHOS were weakly upregulated by *Kmt2d* loss (Figure 2I). These results and others described below prompted us to delve into the regulation of glycolytic genes by KMT2D.

It has been shown that tumorigenesis is promoted by upregulation of glycolysis by ENO1 (Capello et al., 2011), PGK1 (Li et al., 2016), PGAM1 (Hitosugi et al., 2012), LDHA (Sheng et al., 2012), and GAPDH (Colell et al., 2009). CDK1 is a cell-cycle-associated gene (Malumbres and Barbacid, 2009) and increases glycolysis (Wang et al., 2017b). Glycolytic enzymes are considered to be potential therapeutic targets for cancer treatment (Capello et al., 2011; Ganapathy-Kanniappan et al., 2013). In line with the aforementioned mRNA expression data, immunofluorescence (IF) and IHC analysis showed that *Kmt2d* loss increased ENO1, PGK1, and PGAM1 levels while decreasing KMT2D levels (Figures 3A–3C). Analysis of a human LUAD dataset showed that *ENO1*, *PGK1*, *PGAM1*, *LDHA*, and *GAPDH* mRNA levels negatively correlated with *KMT2D* mRNA levels in human LUAD samples (Figure 3D). Moreover, high mRNA levels of *ENO1*, *PGK1*, *PGAM1*, *LDHA*, and *GAPDH* were associated with poor survival in LUAD patients (Figure 3E). These results indicate the human relevance of our findings that *Kmt2d* loss upregulates expression of glycolytic genes in mouse LUAD.

Kmt2d Loss Globally Reduces Super-Enhancer Signals but Has No Obvious Effect on H3K4me3 and H3K27me3 Signals in Mouse Lung Tumors

We and others have shown that KMT2D can catalyze monomethylation, dimethylation, and trimethylation at H3K4 (Dhar et al., 2012; Herz et al., 2012; Lee et al., 2007b, 2013; Zhang et al., 2015b). Monomethyl H3K4 (H3K4me1), together with acetyl H3K27 (H3K27ac), marks enhancers, which spatiotemporally activate gene expression in various locations (Smith and Shilatifard, 2014). KMT2D is required for enhancer formation regulated by the H3K27 acetyltransferases CBP and p300 (Lai et al., 2017; Wang et al., 2017a). We and others have also shown that KMT2D interacts with the H3K27me3 demethylase UTX (Cho et al., 2007;

(B) Pathways upregulated by *Kmt2d* loss in KRAS-driven mouse LUAD. FDR, false discovery rate.

(C and D) Enrichment plot of glycolytic (C) and OXPHOS (D) genes in *Kras*;$Kmt2d^{-/-}$ tumors compared with *Kras* tumors. Each of the black bars represents a gene in the pathway.

(E) Pathways downregulated by *Kmt2d* loss in KRAS-driven mouse LUAD.

(F) Pathways upregulated in human LUAD samples bearing low *KMT2D* mRNA expression (n = 20) or KMT2D-inactivating mutations (n = 4) compared with human LUAD samples (n = 24) bearing high *KMT2D* mRNA expression.

(G and H) Enrichment plot of glycolytic (G) and OXPHOS (H) genes in human LUAD samples bearing low *KMT2D* mRNA expression or KMT2D inactivation compared with human LUAD samples bearing high *KMT2D* mRNA expression.

(I) Analysis of mRNA levels of glycolytic genes and OXPHOS genes in *Kras* and *Kras*;$Kmt2d^{-/-}$ lung tumors using quantitative RT-PCR (n = 3).

In (B) to (H), gene set enrichment analysis was performed and the Benjamini-Hochberg procedure was used for statistical analyses. Data are presented as the mean ± SEM (error bars) of at least three independent experiments or biological replicates. $^{*}p < 0.05$, $^{**}p < 0.01$ (two-tailed Student's t test). See also Tables S1 and S2.

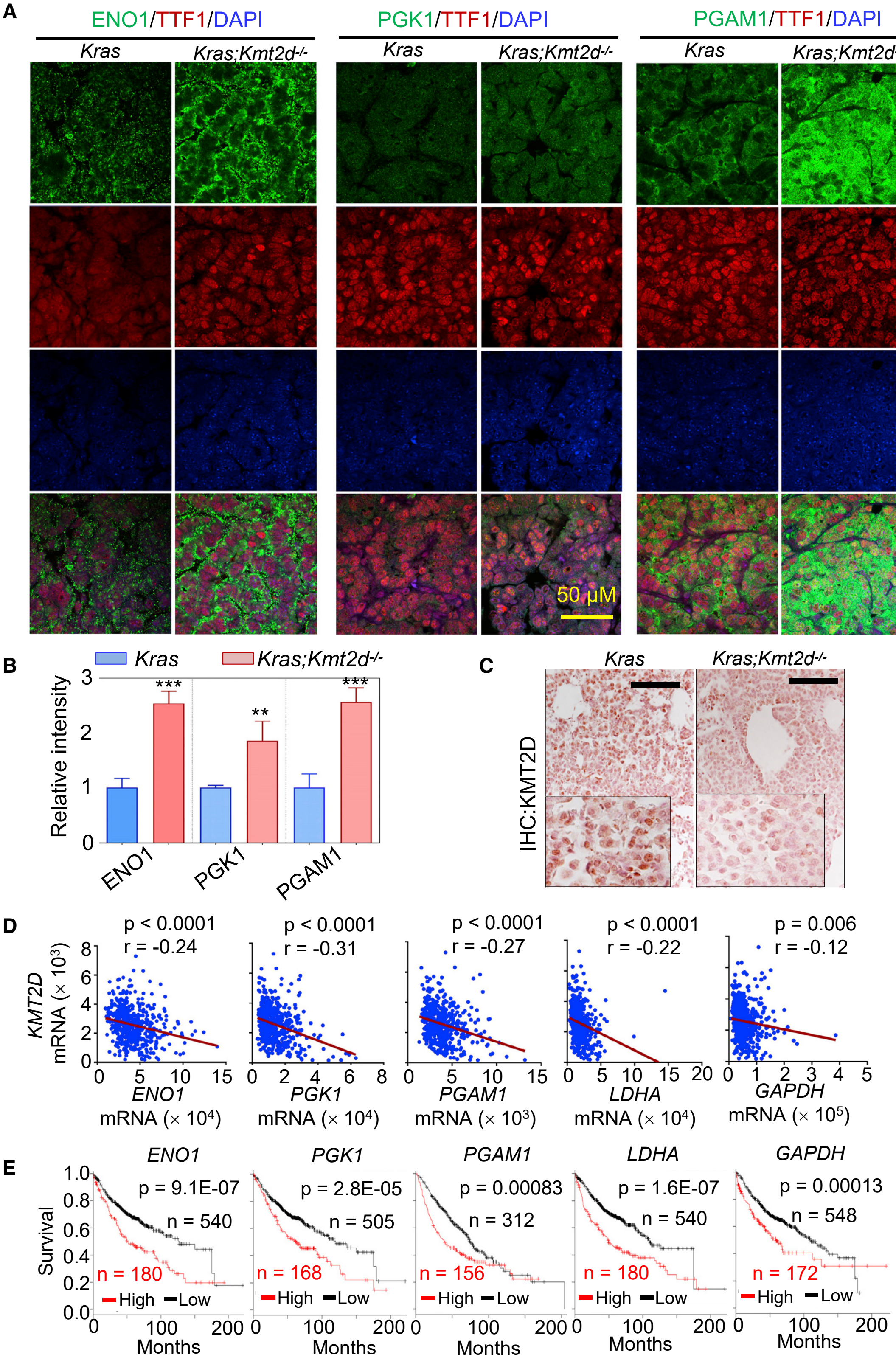

(legend on next page)

Issaeva et al., 2007; Lee et al., 2007b). For these reasons, we performed chromatin immunoprecipitation sequencing (ChIP-seq) for H3K4me1, H3K27ac, H3K4me3, and H3K27me3 to analyze the effect of *Kmt2d* loss on epigenomic landscapes and chromatin states in *Kras* tumors. In the ChIP-seq experiment, we also included H3K79me2 and H3K9me3 because H3K79me2 is associated with transcriptional elongation and H3K9me3 is a marker for heterochromatin (Hawkins et al., 2010; Nguyen and Zhang, 2011). We modeled combinatorial patterns of the six histone modifications using the ChromHMM algorithm (Ernst and Kellis, 2012) and categorized the data into ten different states, as shown in Figure 4A. We noted three prominent transitions in chromatin states from *Kras* tumors to *Kras*;*Kmt2d*$^{-/-}$ tumors: E2 (Active enhancer) to E3 (Weak enhancer), E3 to E9 (Low state = very low signal), and E5 (Active enhancer containing low H3K4me1) to E7 (H3K27ac-lacking transcribed enhancer) (Figures 4B and S3A). Further analysis showed that *Kmt2d* loss did not have any obvious effect on ChIP-seq signals of H3K4me3 and H3K27me3 marks (Figures S3B–S3G). In agreement with these data, IF analyses showed that global levels of H3K4me1 and H3K27ac, but not H3K4me3, were downregulated by *Kmt2d* loss (Figure S3H). These results indicate that *Kmt2d* loss has a strong negative impact on enhancer states.

It has been documented that enhancers can be categorized as super-enhancers and typical enhancers (Whyte et al., 2013). Super-enhancers are characterized by clusters of enhancers that are much larger than typical enhancers with a median size of 0.7–1.3 kb, and highly activate gene expression (Loven et al., 2013; Whyte et al., 2013). Interestingly, our enhancer analysis showed that *Kmt2d* loss strongly decreased average H3K4me1 and H3K27ac levels in super-enhancers and to a lesser extent in typical enhancers (Figures 4C–4F and S4A–S4D). Expression levels of lung-enriched, super-enhancer-associated genes were downregulated by *Kmt2d* loss (Figures S4E and S4F).

Pharmacological Inhibition of Glycolysis Impedes the Tumorigenic Growth of LUAD Cell Lines with KMT2D-Inactivating Mutations

As described above, *Kmt2d* loss upregulated glycolysis program but decreased H3K27ac levels. This led us to test whether the inhibition of glycolytic pathways or H3K27 deacetylation would impede the growth of human lung cancer cell lines bearing loss-of-function mutations in *KMT2D*. To inhibit glycolysis, we used the following inhibitors: 2-deoxy-D-glucose (2-DG), a hexokinase inhibitor and glucose analog (Huang et al., 2015; Pelicano et al., 2006); POMHEX, an enolase inhibitor (Lin et al., 2018); koningic acid (KA), a selective inhibitor of GAPDH (Liberti et al., 2017); lonidamine, a hexokinase and mitochondrial respiration inhibitor (Brawer, 2005); and dinaciclib, an inhibitor of CDK1 and CDK2/5/9 (Parry et al., 2010; Santo et al., 2010). We also tested the OXPHOS inhibitor IACS-010759 (Molina et al., 2018) because *Kmt2d* loss somewhat upregulated the OXPHOS program. To increase histone acetylation via inhibition of histone deacetylase (HDAC), we used AR-42 and vorinostat (also known as SAHA), which has been approved for cancer treatment by the US Food and Drug Administration (Bjornsson et al., 2014; Jacob et al., 2012). We compared the inhibitory effects of these agents on cell confluency of human LUAD cell lines with wild-type (WT) *KMT2D* (A549, H1792, H23, H1437, and H358) and human LUAD cell lines bearing KMT2D-truncating mutations (i.e., H1568, with a nonsense mutation at E758; DV-90, with the truncating mutation P2118fs; and CORL-105, with the truncating mutation R2188fs) (Table S3). Of note, glucose uptake, lactate excretion, and glycolysis metabolites (e.g., glucose-6-phosphate, fructose-6-phosphate, glucose-1,6-bisphosphate, and fructose-1,6-bisphosphate) tended to be higher in the *KMT2D*-mutant cell lines than in the *KMT2D*-WT cell lines (Figures S5A–S5C). 2-DG (and to a lesser extent POMHEX, KA, and vorinostat) inhibited the confluency of the *KMT2D*-mutant cell lines to a greater extent than that of the *KMT2D*-WT cell lines (Figures 5A and 5B). In contrast, AR-42, lonidamine, dinaciclib, and IACS-010759 did not exert an obvious selective inhibition against the confluency of the *KMT2D*-mutant cell lines (Figures S5D–S5G).

Because 2-DG most selectively inhibited cell confluency of the *KMT2D*-mutant LUAD cell lines over several *KMT2D*-WT cell lines, we used 2-DG for subsequent experiments. We tested the effect of 2-DG on cell death. Consistent with the notion that 2-DG can induce cell death in a cell-type- and dose-dependent manner (Zhang et al., 2014), 2-DG induced more cell death in the three *KMT2D*-mutant cell lines than in two *KMT2D*-WT cell lines tested (Figure S5H). In addition, 2-DG tended to inhibit the extracellular acidification rates (ECARs; an indicator for glycolysis) of the *KMT2D*-mutant cell lines to a greater extent than those of the *KMT2D*-WT cell lines (Figures S5I and S5J). We also tested the effect of 2-DG on the growth of the lung cancer cell line LKR10, which is derived from a mouse *Kras*^{G12D} tumor. A three-dimensional (3D) cell-culture system was used, because (1) it better mimics an *in vivo* situation than a 2D culture system does and (2) KMT2D knockdown increased the sizes of the spheroids formed from LKR10 cells in the 3D culture (Figure S6A). In contrast, KMT2D knockdown decreased the proliferation of

Figure 3. High Expression Levels of Several Glycolytic Genes Negatively Correlate with *KMT2D* mRNA Levels in LUADs and Are Linked to Poor Prognosis in LUAD Patients

(A and B) Immunofluorescence (IF) analysis for ENO1, PGK1, and PGAM1 in *Kras* and *Kras*;*Kmt2d*$^{-/-}$ lung tumor tissues. Representative IF images are shown (A), and the IF images were quantified (B). TTF1 is an LUAD marker. Data are presented as the mean ± SEM (error bars) of at least three independent experiments or biological replicates. $^{**}p < 0.01$, $^{***}p < 0.001$ (two-tailed Student's t test).

(C) IHC analysis for KMT2D in *Kras* and *Kras*;*Kmt2d*$^{-/-}$ lung tumor tissues. Scale bars, 50 μm.

(D) Inverse correlations of *KMT2D* mRNA levels with *ENO1*, *PGK1*, *PGAM1*, *LDHA*, and *GAPDH* mRNA levels in human LUADs in the TCGA dataset (n = 517). Statistical analysis was performed using two-tailed Student's t test. r, Pearson's correlation coefficient.

(E) Kaplan-Meier survival analysis of human LUAD patients using *ENO1*, *PGK1*, *PGAM1*, *LDHA*, and *GAPDH* mRNA levels. Higher quartile (except a best cutoff for *PGAM1* data) was used as a cutoff to divide the samples into high (the highest 25%) and low (the remaining 75%) groups in the KM Plotter database (http://kmplot.com/analysis). Statistical analysis was performed using the two-sided log-rank test. *KMT2D* probe set, 227527_at; *ENO1* probe set, 201231_at; *PGK1* probe set, 227068_at; *PGAM1* probe set, 200886_at; *LDHA* probe set, 200650_s_at; *GAPDH* probe set, 212581_at.

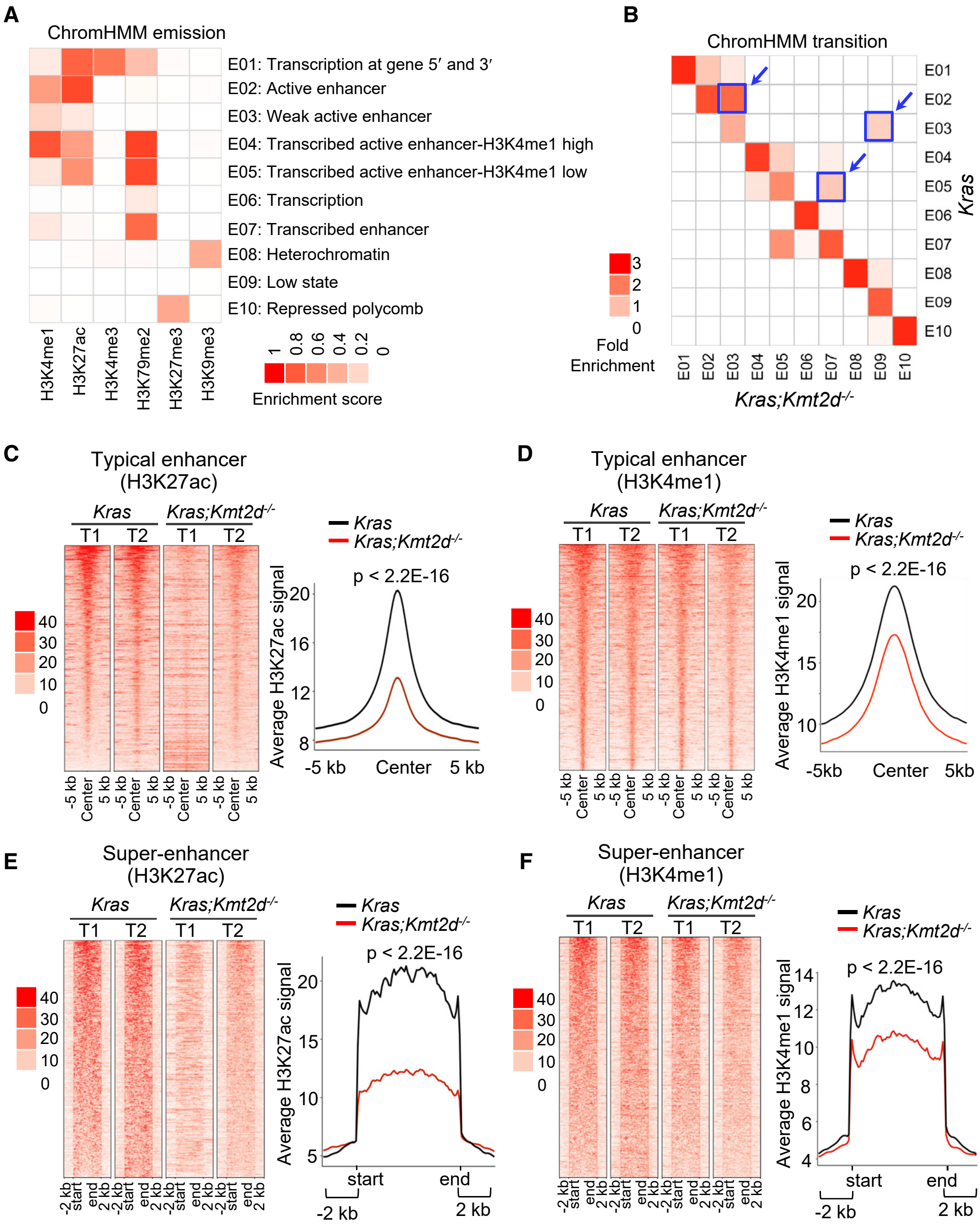

Figure 4. *Kmt2d* Loss Reduces Epigenomic Signals for Super-Enhancers and to a Lesser Extent Typical Enhancers at the Genome-Wide Level

(A) Emission probabilities of the 10-state ChromHMM model calculated from six histone modification profiles in *Kras* and *Kras*;*Kmt2d*$^{-/-}$ lung tumors. Each row represents one chromatin state. The 10 states predicted using ChromHMM represent various enhancer states (E2, E3, E4, E5, and E7), promoter state (E1), transcription states (E1, E6, and E7), polycomb-repressed state (E10), and heterochromatin state (E8). Each column corresponds to a histone modification. The intensity of the color in the scale from 0 (white) to 1 (red) in each cell reflects the frequency of occurrence of each histone mark in the indicated chromatin state.

(B) Heatmap showing the fold enrichment of transitions of chromatin states from *Kras* lung tumors to *Kras*;*Kmt2d*$^{-/-}$ lung tumors. The color intensities represent the relative fold enrichment.

(C and D) Heatmaps (left panels) and average intensity curves (right panels) of ChIP-seq reads (RPKM; reads per kilobase of transcript per million mapped reads) for H3K27ac (C) and H3K4me1 (D) at typical enhancer regions. Enhancers are shown in a 10-kb window (centered on the middle of the enhancer) in *Kras* and *Kras*;*Kmt2d*$^{-/-}$ lung tumors.

(E and F) Heatmaps (left panels) and average intensity curves (right panels) of ChIP-seq reads for H3K27ac (E) and H3K4me1 (F) at the super-enhancer regions plus their flanking 2-kb regions in *Kras* and *Kras*;*Kmt2d*$^{-/-}$ lung tumors.

Wilcoxon rank-sum test was used for statistical analysis of (C) to (F). T1, tumor 1; T2, tumor 2. See also Figures S3 and S4.

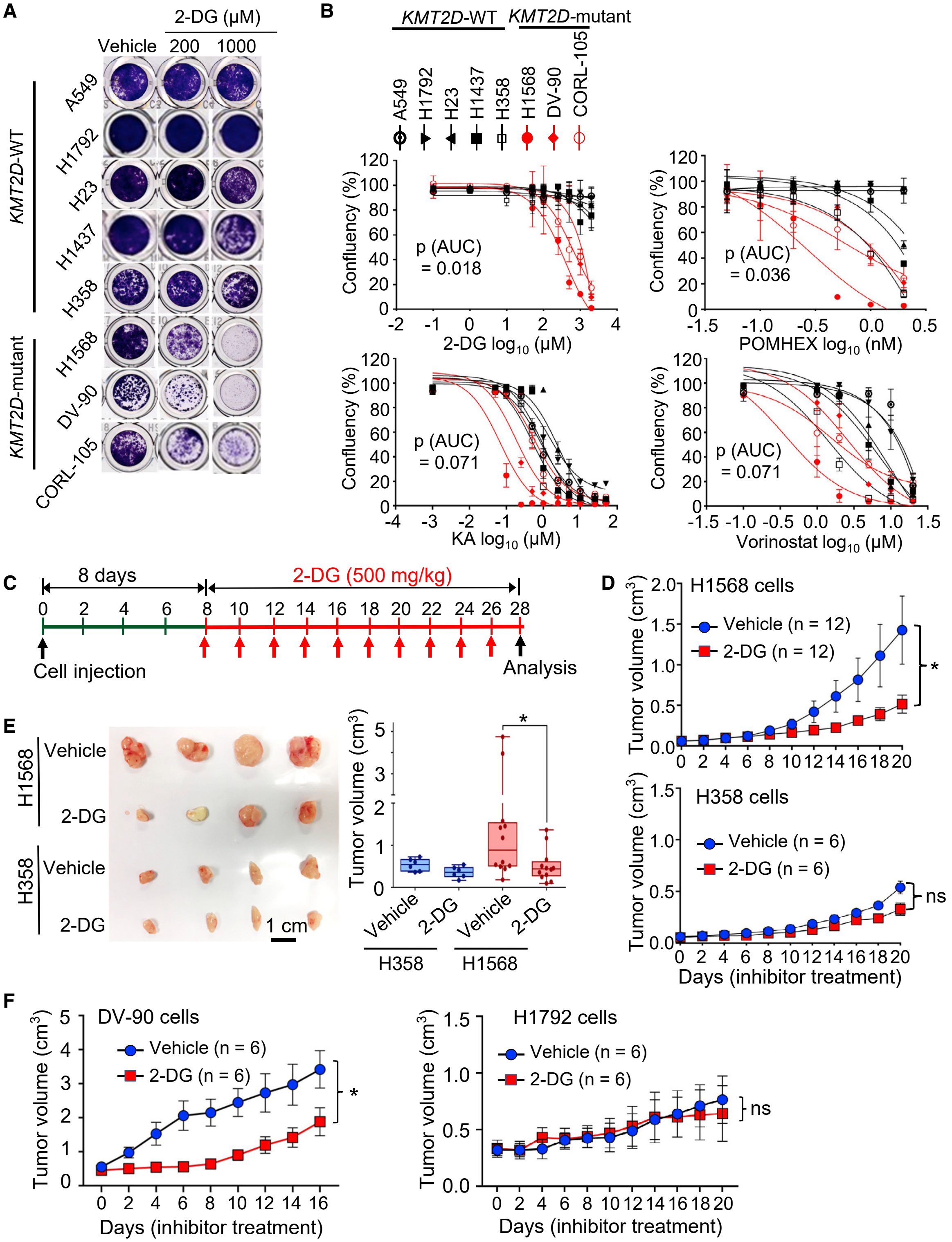

Figure 5. Inhibition of Glycolysis Suppresses Tumorigenic Growth of *KMT2D*-Mutant LUAD Cell Lines

(A and B) Effect of 2-deoxy-D-glucose (2-DG) on the confluency of human LUAD cell lines bearing WT *KMT2D* (A549, H1792, H23, H1437, and H358) and LUAD cell lines bearing KMT2D-truncating mutations (H1568, DV-90, and CORL-105) (A) and dose-response curves of several inhibitors on these LUAD cell lines (B). Cells were treated with various concentrations of the hexokinase inhibitor 2-DG, the enolase inhibitor POMHEX, the GAPDH inhibitor KA, and the HDAC inhibitor SAHA/vorinostat. Wilcoxon rank-sum test (n = 3) was used for statistical analysis. AUC, area under the curve.

(legend continued on next page)

several LUAD cell lines in the 2D culture system (data not shown). In line with its inhibitory effect on confluency of human LUAD cells, 2-DG inhibited spheroid growth of KMT2D-depleted LKR-10 cells to a greater extent than that of shLuciferase-treated LKR-10 cells (control) in the 3D culture system (Figures S6A and S6B).

To examine whether 2-DG selectively inhibits tumorigenic growth of *KMT2D*-mutant LUAD cells over *KMT2D*-WT LUAD cells, we used H1568 cells harboring a KMT2D-truncation mutation and H358 cells harboring WT *KMT2D*. H1568 cells and H358 cells have similar proliferation rates in 2D cultures (Figure S6C). Notably, 2-DG preferentially inhibited the tumorigenicity of *KMT2D*-mutant H1568 cells compared with *KMT2D*-WT H358 cells in a mouse subcutaneous xenograft model (Figures 5C–5E). However, KA, which less selectively inhibited *KMT2D*-mutant cell lines than did 2-DG, weakly and insignificantly impeded the tumorigenicity of H1568 cells compared with H358 cells (Figures S6D and S6E). Using another KMT2D-truncated cell line DV-90 and another *KMT2D*-WT cell line H1792, we compared the *in vivo* inhibitory effect of 2-DG on their tumorigenic growth. H1792 cells grew faster than DV-90 cells in a 2D culture (Figure S6C), but DV-90 cells formed tumors faster than H1792 cells in a mouse xenograft model (Figure 5F). In agreement with the above results, 2-DG selectively inhibited tumorigenic growth of *KMT2D*-mutant DV-90 cells over *KMT2D*-WT H1792 cells (Figure 5F). Finally, to test the effect of 2-DG on the tumorigenicity of *KMT2D*-WT and *KMT2D*-mutant LUAD cells in an isogenic cell state, we generated *KMT2D*-mutant H1568 cells harboring doxycycline (Dox)-inducible WT *KMT2D* (Figure S6F) and then compared the inhibitory effect of 2-DG on tumorigenic growth of these cells between Dox treatment and no Dox treatment. *KMT2D* induction decreased ECAR (Figure S6F). In line with the above results, 2-DG tended to preferentially impede tumorigenic growth of *KMT2D*-inducible H1568 cells in Dox-untreated mice compared with Dox-treated mice (Figure S6G). These results suggest that increased glycolysis in *KMT2D*-mutant LUAD tumors can be targeted by the glycolysis inhibitor 2-DG.

KMT2D Is Required for the Activity of the *Per2* Super-Enhancer, and PER2 Represses Glycolytic Genes

Because KMT2D is a transcriptional co-activator, *Kmt2d* loss may not directly upregulate a tumor-promoting glycolysis program. Thus, we hypothesized that the glycolysis program upregulated by *Kmt2d* loss may be repressed by a tumor-suppressive, transcription-repressive regulator encoded by a KMT2D-activated gene (i.e., a gene downregulated by *Kmt2d* loss). To identify such a regulator, we first searched the genes that were both downregulated by *Kmt2d* loss (n = 522) and associated with significant decreases in H3K27ac levels (n = 3,751), because *Kmt2d* loss strongly downregulated the enhancer mark H3K27ac to decrease gene expression (Figures 6A and 6B). To further reduce the number of candidate regulators, we incorporated aspects of human lung cancer into our analysis. Specifically, we examined which genes among those downregulated by *Kmt2d* loss correlate with *KMT2D* mRNA levels in more than 0.3 of the correlation coefficient value (r) in human LUAD samples in the TCGA dataset. This analysis resulted in 14 candidate genes (Figures 6C and S7A). Of note, *Kmt2d* loss in KRAS-driven lung tumors did not affect expression of *Dnmt3a* (a transcriptional co-repressor gene) and DNMT3A-regulated Ras activator genes (*Rasgrp1*, *Rasgrf1*, *Rasgrf2*, *Rapgef5*, and *Rgl1*) (Figure S7B), although expression of *Dnmt3a* was downregulated by *Kmt2d* loss in other types of tumors (e.g., medulloblastoma) (Dhar et al., 2018). Of these 14 genes, expression levels of five (*SHANK2*, *ACACB*, *PER2*, *NFASC*, and *CLCN6*) were lower in LUAD tumors than in adjacent normal tissues, and their low levels correlated with poor prognosis in lung cancer patients (Figures 6D–6F and S7C–S7G).

Of these five genes, the circadian rhythm repressor gene *Per2* was particularly interesting for the following reasons: (1) *Per2* loss in mouse lung promoted lung tumorigenesis (Papagiannakopoulos et al., 2016); (2) *Per2* loss increased glucose metabolism, implicating PER2 in regulation of glycolysis (Papagiannakopoulos et al., 2016); and (3) disruption of circadian rhythm increased the tumorigenicity (Filipski et al., 2003; Fu et al., 2002). As aforementioned and also shown in Figures 7A and 7B, *Kmt2d* loss decreased *Per2* expression levels, and *PER2* mRNA levels significantly correlated with *KMT2D* mRNA levels. *Kmt2d* loss also reduced PER2 protein levels (Figure 7C). Interestingly, *Per2* was occupied by a large cluster of H3K4me1 and H3K27ac peaks that are indicative of a super-enhancer (Figures 7D and 7E). In enhancer regions, RNAs called enhancer RNAs (eRNAs) are bidirectionally transcribed by RNA Polymerase II, and enhancer activities can be assessed by eRNA levels (Kim and Shiekhattar, 2015). Therefore, we measured the effect of *Kmt2d* loss on eRNA levels in the *Per2*–associated super-enhancer. *Kmt2d* loss decreased eRNA levels in the super-enhancer region, suggesting that *Kmt2d* loss reduces the activity of the *Per2* super-enhancer (Figure 7F).

To further assess the role of the KMT2D-PER2 pathway in repressing glycolytic genes that are upregulated by *Kmt2d* loss, we used the mouse *Kras* LUAD cell line LKR10. ChIP results showed that KMT2D occupied the *Per2* gene in LKR10 cells (Figure 7G). ChIP results also showed that PER2 occupied several glycolytic genes (e.g., *Eno1*, *Pgk1*, *Pgam1*, *Ldha*, *Gapdh*, and *Cdk1*) and that KMT2D knockdown reduced PER2 occupancy in these genes (Figures 7H and S7H). Similar to the effect of *Kmt2d* loss on glycolytic genes in *Kras* tumors, our RNA-seq and qRT-PCR data showed that KMT2D

(C–E) Effect of 2-DG on tumorigenic growth of H1568 cells bearing a KMT2D-truncating mutation and of H358 cells bearing WT *KMT2D* in a mouse subcutaneous xenograft model. The schedule of treatment of mice with 2-DG is shown (C). The sizes of xenograft tumors after treatment with 2-DG or vehicle control were measured (D). Tumors were dissected from the mice (E). In the box plots, the bottom and the top rectangles indicate the first quartile (Q1) and third quartile (Q3), respectively. The horizontal lines in the middle signify the median (Q2), and the vertical lines that extend from the top and the bottom of the plot indicate the maximum and minimum values, respectively.

(F) Effect of 2-DG on tumorigenic growth of DV-90 cells bearing a KMT2D-truncating mutation and of H1792 cells bearing WT *KMT2D* in a mouse subcutaneous xenograft model. Mice were treated with 2-DG (500 mg/kg body weight every other day) or vehicle.

ns indicates non-significant. *p < 0.05 (two-tailed Student's t test). See also Figures S5 and S6; Table S3.

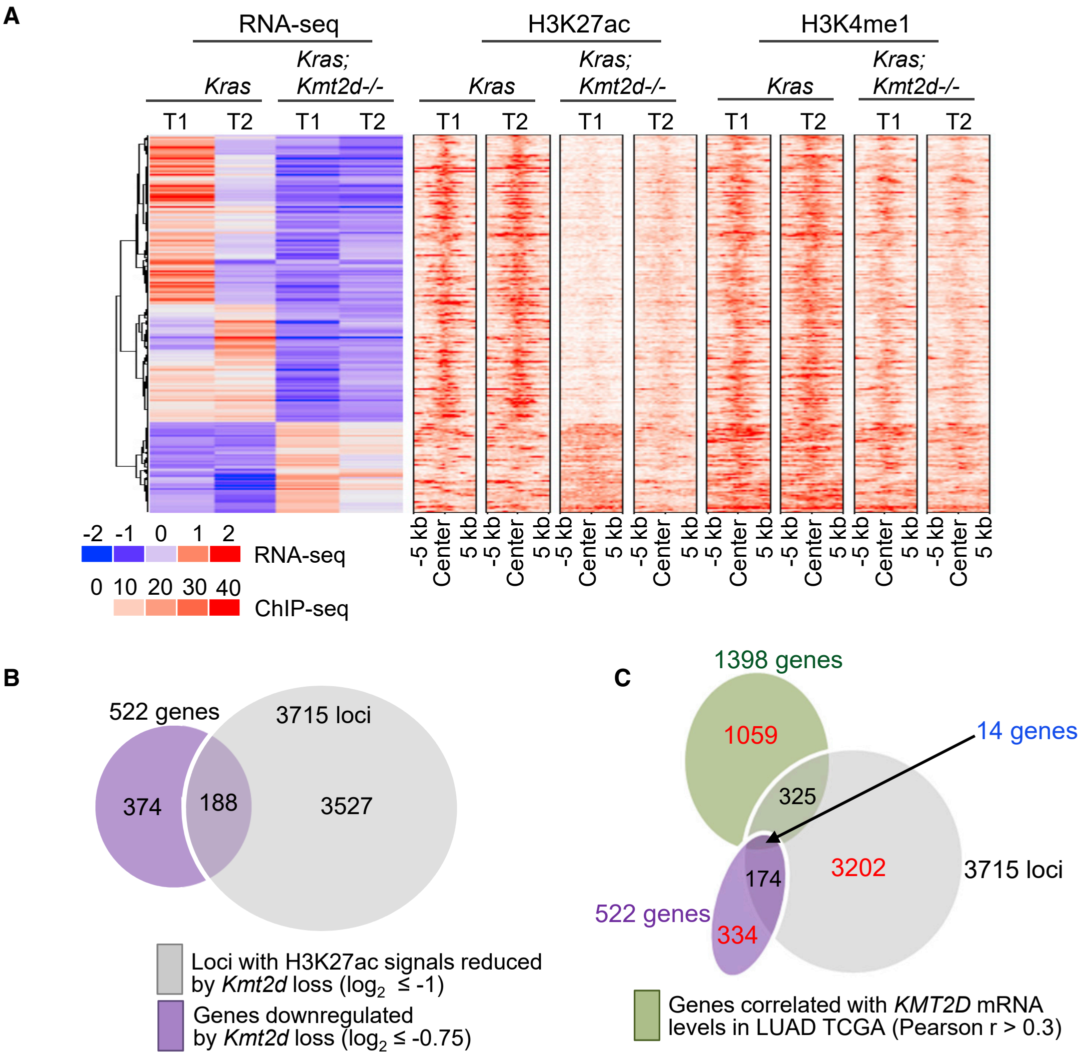

D

	Fold change in RNA-seq by *Kmt2d* loss ($\log_2$)	Correlation with *KMT2D* mRNA (r)	Fold change in H3K27ac signal ($\log_2$)	Fold change in mRNA expression (LUAD/Normal)	Survival p value
SHANK2	-2.0252	0.49	-4.28972	0.596	1.4E-10
ACACB	-1.16118	0.53	-2.72969	0.312	1.2E-05
PER2	-0.92642	0.32	-1.66447	0.77	4.2E-11
NFASC	-0.89593	0.3	-2.22851	0.27	0.0043
CLCN6	-0.86943	0.48	-2.27149	0.675	3.6E-06

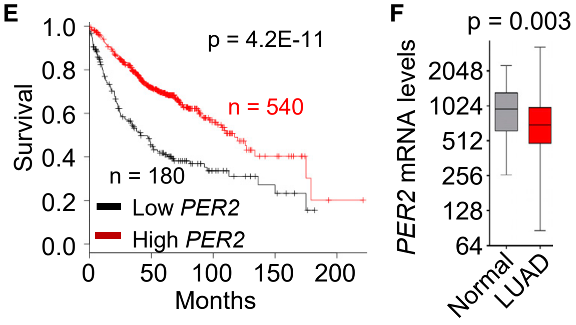

Figure 6. Integrative Analysis of Expression, Enhancers, and Clinical Relevance for KMT2D-Regulated Genes

(A) Heatmaps for genes differentially expressed between *Kras* and *Kras*;*Kmt2d*$^{-/-}$ lung tumors and for the signals of their closest H3K27ac and H3K4me1 peaks.

(B) Venn diagram showing the overlap between genes downregulated by *Kmt2d* loss (n = 522) and genes with H3K27ac ChIP-seq signals reduced by *Kmt2d* loss (n = 3,715).

(C) Venn diagram showing the overlap between genes downregulated by *Kmt2d* loss (n = 522), genes with H3K27ac ChIP-seq signals reduced by *Kmt2d* loss (n = 3,715), and genes correlated with *KMT2D* expression (n = 1,398 with r ≥ 0.3) in LUAD samples (n = 357) in the TCGA database.

(legend continued on next page)

knockdown in LKR10 cells robustly upregulated expression levels of the glycolytic genes while downregulating *Per2* expression (Figures 8A and S8A). In line with this, KMT2D knockdown increased glucose uptake, lactate excretion, several glycolysis metabolites (e.g., glucose-6-phosphate, fructose-6-phosphate, glucose-1,6-bisphosphate, and fructose-1,6-bisphosphate), and ECARs in LKR10 cells (Figures 8B, S8B, and S8C). Of note, KMT2D knockdown increased expression of OXPHOS genes and oxygen consumption rate to a lesser extent than expression of glycolytic genes and ECARs (Figures S8C and S8D). To verify the effect of KMT2D knockdown on glycolytic genes, we ectopically expressed in KMT2D-depleted cells a functional but smaller KMT2D (herein called mini-KMT2D), which rescued the differentiation defect of KMT2D-depleted cells in our previous study (Dhar et al., 2012) and upregulated gene expression via enhancer activation in another study (Wang et al., 2017a). This rescue experiment demonstrated that mini-*KMT2D* expression restored *Per2* expression as well as eRNA and H3K27ac levels for the *Per2* super-enhancer while repressing expression of *Eno1*, *Pgk1*, *Pgam1*, *Ldha*, *Gapdh*, and *Cdk1* (Figures 8C and 8D). Consistent with this, Dox-induced expression of *KMT2D* in human H1568 cells increased *PER2* expression while decreasing expression of glycolytic genes, glucose uptake, lactate excretion, and the spheroid growth (Figures 8E, 8F, and S8E). These results suggest that KMT2D directly upregulates *Per2* expression by activating the *Per2* super-enhancer and that KMT2D-upregulated PER2 represses glycolytic genes.

To convincingly confirm the regulation of glycolytic genes by PER2, we examined the effect of *PER2* overexpression and PER2 knockdown on expression of glycolytic genes (e.g., *Eno1*, *Pgk1*, *Pgam1*, *Ldha*, *Gapdh*, and *Cdk1*) in LKR10 cells. *PER2* overexpression decreased expression of these genes (Figure 8G). PER2 knockdown increased their expression levels and ECAR while slightly increasing expression of several OXPHOS genes (Figures 8H, S8F, and S8G). In agreement with gene expression data, enzyme assays showed that PER2 (or KMT2D) knockdown increased ENO1 and GAPDH activities whereas *PER2* (or *KMT2D*) overexpression decreased their activities (Figure S8H). *PER2* expression levels negatively correlated with expression of several glycolytic genes (*ENO1*, *PGK1*, *PGAM1*, *LDHA*, and *CDK1*) in a TCGA LUAD dataset (Figure 8I). Finally, we examined the effect of ectopic expression of *PER2* on the spheroid growth of KMT2D-depleted LKR10 cells. *PER2* expression decreased the spheroid growth of these cells in the 3D culture system (Figure S8I). These results, together with the above results, indicate that the tumor-suppressive function of KMT2D is dependent, at least in part, on the downregulation of glycolytic genes by PER2.

DISCUSSION

In the present study, our results indicate that KMT2D acts as an epigenetic LUAD suppressor by positively regulating super-enhancers (e.g., *Per2* super-enhancer) and thereby increasing expression of the tumor-suppressor gene *Per2*. In addition, our findings indicate that KMT2D-mediated upregulation of *Per2* represses tumor-promoting glycolytic genes and that KMT2D defectiveness or deficiency decreases *Per2* expression to upregulate glycolytic genes. Our *in vitro* and *in vivo* experiments showed that increased glycolysis in KMT2D-defective lung cancer cells could be targeted by pharmacological inhibition. Interestingly, the glycolysis pathway is enriched not only in our *Kras*;$Kmt2d^{-/-}$ tumor model over *Kras* model but also in human LUAD tumors with low/mutant *KMT2D* over those with high WT *KMT2D*. In this aspect, the *Kras*;$Kmt2d^{fl/fl}$ mouse model represents an epigenetic LUAD mouse model and may be useful for future studies of human LUAD.

It has been reported that KMT2D is required for the formation of acute myeloid leukemia by the MLL-AF9 oncogene (Santos et al., 2014) and for HOXA9/MEIS1-mediated leukemogenesis (Sun et al., 2018). In contrast, results reported here showed that lung-specific deletion of *Kmt2d* significantly promoted KRAS-driven lung tumorigenesis in mice and shortened the survival of mice bearing KRAS-driven tumors, suggesting that *Kmt2d* loss cooperates with other oncogenic aberrations (e.g., *Kras* activation) to increase LUAD tumorigenicity. The lung tumor-suppressive function of KMT2D is further supported by our following additional results: (1) *Kmt2d* loss upregulated expression of tumor-promoting glycolytic genes, such as *Eno1*, *Pgk1*, *Pgam1*, *Ldha*, and *Gapdh*; (2) *Kmt2d* loss downregulated tumor-suppressive genes, such as *Per2*; and (3) KMT2D depletion increased sizes of spheroids formed by lung cancer cells in the 3D culture system. In line with the tumor-suppressive function of KMT2D, we have recently shown that brain-specific *Kmt2d* loss alone induces spontaneous medulloblastoma (cerebellar tumor) in brain (Dhar et al., 2018). Our and other studies indicate that KMT2D acts as a tumor suppressor in melanoma (Maitituoheti et al., 2018) and pancreatic cancer cells (Koutsioumpa et al., 2019). Furthermore, additional studies have demonstrated that genetic ablation of *Kmt2d* in B cells enhanced B cell lymphoma genesis, also indicating KMT2D's tumor-suppressive function (Ortega-Molina et al., 2015; Zhang et al., 2015a). Thus, the anti- or pro-tumorigenicity of KMT2D may be cell-type dependent, although many studies suggest that KMT2D has a tumor-suppressive function in a majority of tissues.

We have recently shown that in medulloblastoma occurred in brain-specific *Kmt2d* knockout mice, *Kmt2d* loss induces Ras signaling pathways by highly increasing expression of several

---

(D) Top five hits on the basis of the five different parameters indicated. r, Pearson's correlation coefficient.

(E) Kaplan-Meier survival analysis showing the association of low *PER2* mRNA levels with poor survival in lung cancer patients. The lower quartile was used as a cutoff to divide the samples into low (the lowest 25%) and high (the remaining 75%) *KMT2D* mRNA groups. *PER2* probe set, 205251_at.

(F) Box plots showing downregulation of *PER2* mRNA levels in LUAD samples (n = 517) compared with their adjacent normal samples (n = 54) in the TCGA dataset. In the box plots, the bottom and the top rectangles indicate the first quartile (Q1) and third quartile (Q3), respectively. The horizontal lines in the middle signify the median (Q2), and the vertical lines that extend from the top and the bottom of the plot indicate the maximum and minimum values, respectively.

In (D) and (E), the p values were calculated using the two-sided log-rank test. In (F), the p values were determined using two-tailed Student's t test. ns indicates non-significant; $*p < 0.05$. See also Figure S7.

Please cite this article in press as: Alam et al., KMT2D Deficiency Impairs Super-Enhancers to Confer a Glycolytic Vulnerability in Lung Cancer, Cancer Cell (2020), https://doi.org/10.1016/j.ccell.2020.03.005

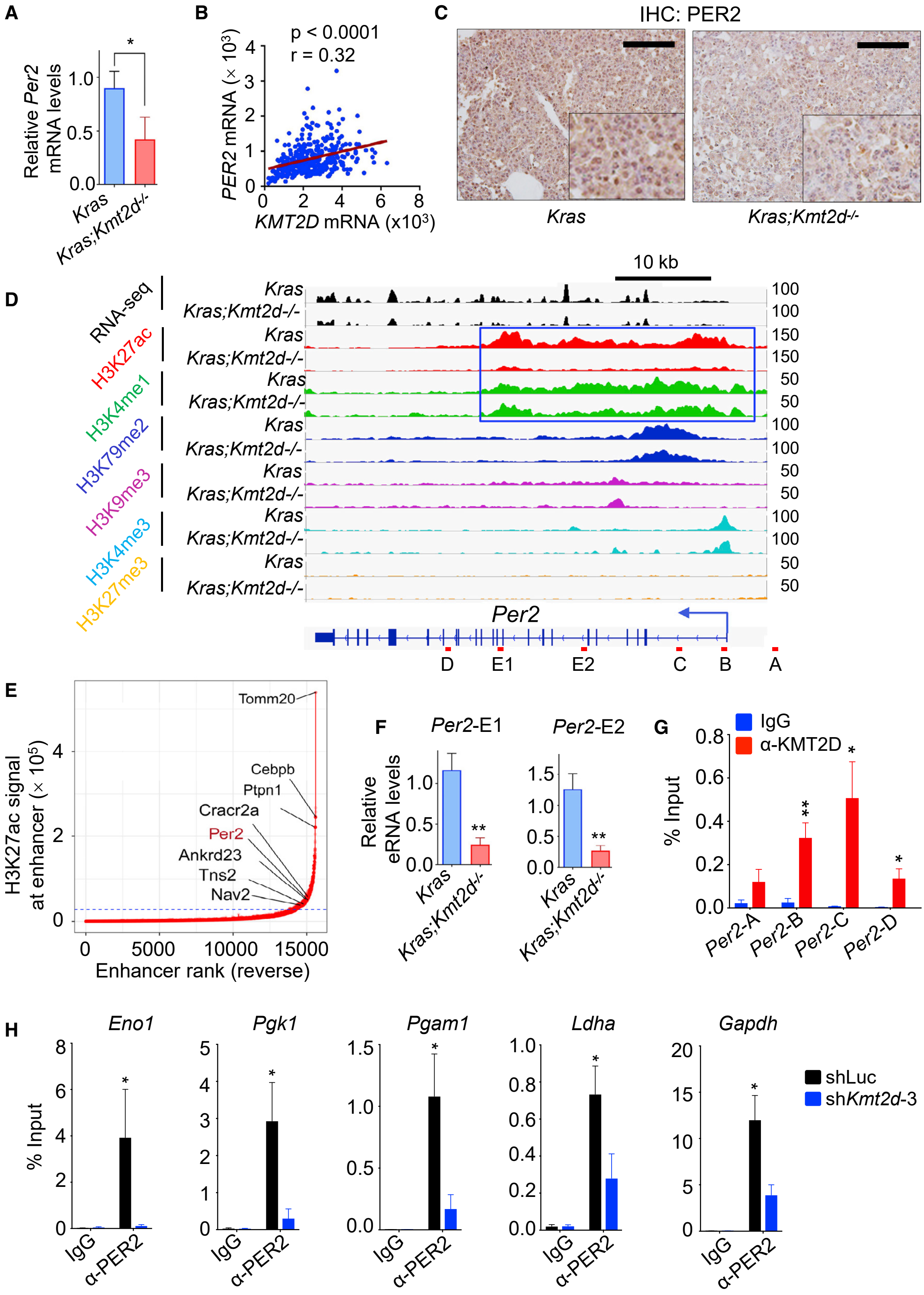

(legend on next page)

Ras activator genes (e.g., *Rasgrp1*, *Rasgrf1*, *Rasgrf2*, *Rapgef5*, and *Rgl1*) (Dhar et al., 2018). In the same study, we have also demonstrated that KMT2D activates expression of the DNA methyltransferase 3A (*Dnmt3a*) and that DNMT3A represses expression of these Ras activator genes. Similar to this, KMT2D knockdown decreased expression of *DNMT3A* expression in human lymphoma cells (Ortega-Molina et al., 2015). In contrast to these studies, the present study showed that *Kmt2d* loss in lung tumorigenesis induced neither expression of Ras activator genes nor decreased *Dnmt3a* expression. Instead, *Kmt2d* loss increased expression of glycolytic genes in lung tumorigenesis. Therefore, it is likely that the tissue variation of tumor-suppressive activity of KMT2D would result from KMT2D-mediated regulation of different gene sets in a tissue-specific manner. Then, how does KMT2D-regulated gene expression occur in a tissue-specific manner? Interestingly, it has been shown that the KMT2D complex interacts with tissue-specific DNA-binding transcription factors. For example, the KMT2D complex co-localizes with MyoD during myocyte differentiation while interacting with PPARγ and C/EBP during adipocyte differentiation (Lee et al., 2013). Thus, a tissue-specific factor may direct the KMT2D complex to a unique set of genes to instruct KMT2D-mediated gene activation in a tissue-dependent manner.

The circadian rhythm repressor PER2 plays an important role in tumor suppression (Filipski et al., 2003; Fu et al., 2002). Results reported here indicate that KMT2D upregulates *Per2* expression and indirectly represses tumor-promoting glycolysis via *Per2* activation. Moreover, our results define several oncogenic glycolytic genes (e.g., *Eno1*, *Pgk1*, *Pgam1*, *Ldha*, *Gapdh*, and *Cdk1*) as target genes of PER2. Therefore, KMT2D-mediated *Per2* activation represents a previously unknown tumor-suppressive mechanism that links an epigenetic tumor suppressor to a circadian rhythm regulator. PER2 moves into the nucleus during the evening and downregulates gene expression by antagonizing the circadian rhythm heterodimeric activator CLOCK:BMAL1. During the night, PER2 is gradually phosphorylated and targeted for ubiquitination that leads to proteasomal degradation (Bass and Takahashi, 2010; Koike et al., 2012). Distinct from this type of PER2 regulation, our results uncover a *Per2*-regulatory mechanism in which KMT2D upregulates *Per2* expression by activating the *Per2* super-enhancer, providing molecular insights into how *Per2* is epigenetically regulated. Super-enhancer formation has been linked to oncogene activation (Sur and Taipale, 2016). However, our results indicate that the *Per2* super-enhancer is associated with tumor-suppressive function in LUAD, consistent with our recent finding that super-enhancer diminution downregulates expression of tumor-suppressor genes against medulloblastoma genesis (Dhar et al., 2018). Taken together, our findings reveal a tumor-suppressive mechanism by which KMT2D indirectly downregulates glycolytic genes by enhancing *Per2* expression via super-enhancer activation and thereby suppresses LUAD.

Increased aerobic glycolysis, known as the Warburg effect, is a major characteristic of cancer cells, providing them with a proliferation advantage by producing ATP as well as glucose-derived metabolites for biosynthesis of nucleotides, lipids, and proteins (Gatenby and Gillies, 2004). Therefore, targeting glycolytic pathways to arrest tumorigenic growth of cancer cells remains an attractive therapeutic intervention. Interestingly, the present study showed that *Kmt2d* loss increased expression of glycolytic genes. Our other study also showed that *Kmt2d* loss increased glycolysis via IGFBP5-regulated IGF (insulin-like growth factor) signaling while promoting melanoma tumorigenesis (Maitituoheti et al., 2018). In line with these findings, we demonstrated that the glycolysis inhibitor 2-DG impeded the tumorigenicity of LUAD cell lines bearing KMT2D-inactivating mutations in a mouse xenograft model. Because *KMT2D* is mutated in several other types of cancer (Suva et al., 2013) and 2-DG has re-entered clinical trials, our findings may rationalize glycolysis inhibition as an anticancer treatment strategy against other cancer types bearing KMT2D-inactivating mutations besides human KMT2D-inactivated LUAD.

STAR★METHODS

Detailed methods are provided in the online version of this paper and include the following:

- KEY RESOURCES TABLE
- LEAD CONTACT AND MATERIALS AVAILABILITY
- EXPERIMENTAL MODEL AND SUBJECT DETAILS
  - Cell Lines
  - Mouse Strains and Genetically Engineered Lung Cancer Mouse Models
  - *In Vivo* Lung Tumorigenesis Study
  - Study Approval
- METHOD DETAILS
  - Micro-Computed Tomography

Figure 7. KMT2D Positively Regulates *Per2* Expression, and PER2 Occupies Glycolytic Genes

(A) Analysis of relative *Per2* mRNA levels in *Kras* and *Kras*;*Kmt2d*$^{-/-}$ lung tumors using qRT-PCR.

(B) Scatterplot showing a positive correlation between *KMT2D* and *PER2* mRNA levels in the TCGA LUAD dataset (n = 517). Statistical analysis was performed using two-tailed Student's t test. r, Pearson's correlation coefficient.

(C) Analysis of PER2 protein levels in *Kras* and *Kras*;*Kmt2d*$^{-/-}$ lung tumors using IHC. Scale bars, 50 μm.

(D) Genome browser view of normalized ChIP-seq signals of six chromatin marks (H3K27ac, H3K4me1, H3K79me2, H3K9me3, H3K4me3, and H3K27me3) at the *Per2* locus in *Kras* and *Kras*;*Kmt2d*$^{-/-}$ lung tumors. All the tracks (except H3K4me3) were the average of two biological replicates. The *Per2*-associated super-enhancer is indicated by the blue-outlined box.

(E) Plot indicating super-enhancers identified on the basis of H3K27ac signals. The numbers on the x axis are in reverse order.

(F) Analysis of eRNA levels for two different regions (E1 and E2) of the *Per2* super-enhancer in *Kras* and *Kras*;*Kmt2d*$^{-/-}$ lung tumors using qRT-PCR.

(G) Quantitative ChIP analysis of KMT2D in *Per2* in LKR10 cells.

(H) Quantitative ChIP analysis of PER2 in glycolytic genes in LKR10 cells. ChIP amplicons are indicated in Figure S7H.

In (A), (F), (G), and (H), data are presented as the mean ± SEM (error bars) of at least three independent experiments or biological replicates. $^{*}p < 0.05$, $^{**}p < 0.01$ (two-tailed Student's t test).

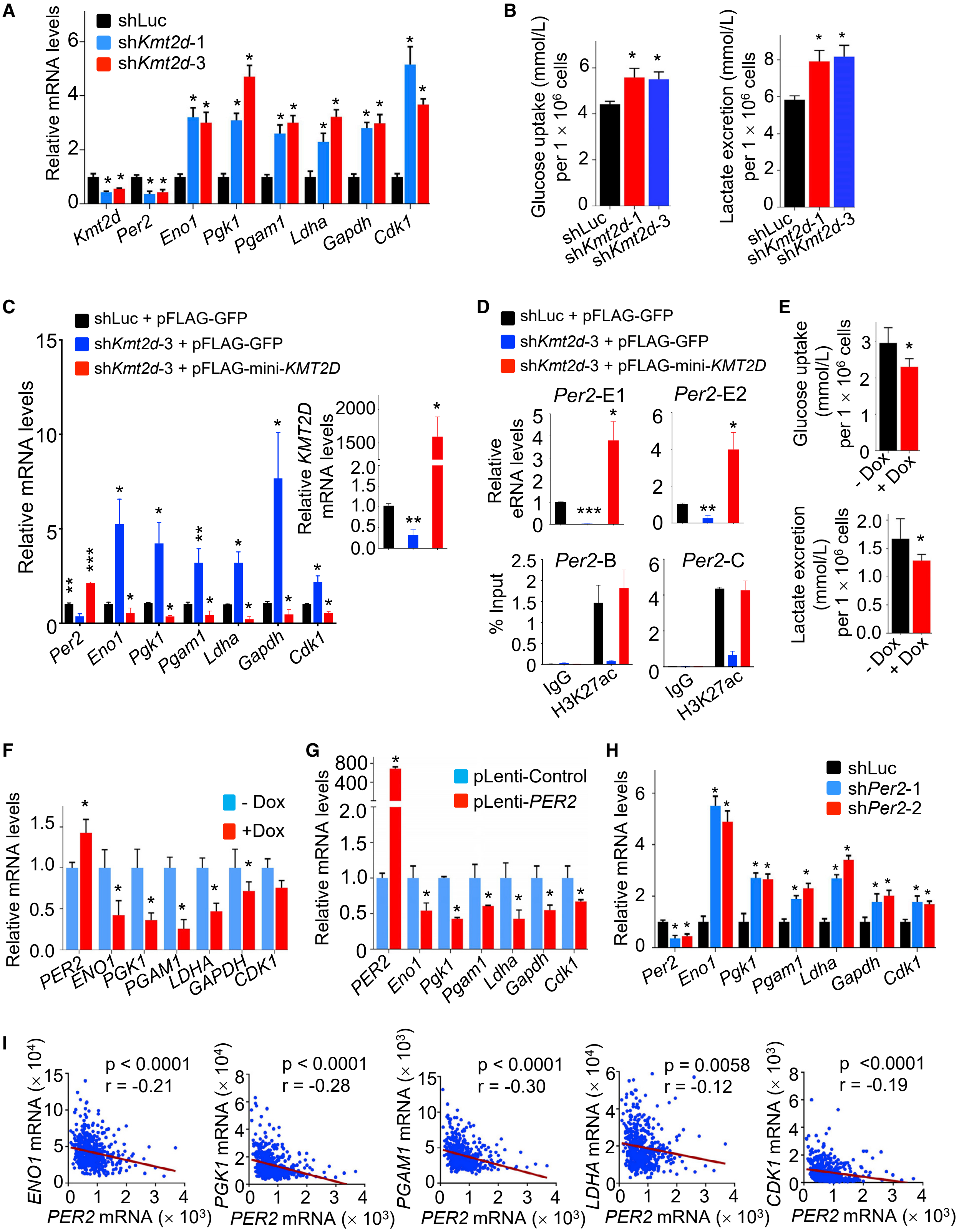

Figure 8. KMT2D-Activated *Per2* Expression Represses Glycolytic Genes

(A) Analysis of the effect of KMT2D knockdown on *Per2*, *Eno1*, *Pgk1*, *Pgam1*, *Ldha*, *Gapdh*, and *Cdk1* mRNA levels in mouse LKR-10 LUAD cells bearing $KRAS^{G12D}$ using qRT-PCR.

(legend continued on next page)

  - ○ Histologic, Immunohistochemical, and Immunofluorescence Analyses
  - ○ Survival Analysis and Gene Expression Correlation Analysis
  - ○ RNA Isolation from Lung Tumor Cells
  - ○ RNA-seq Analysis
  - ○ TCGA RNA-seq Data Analysis
  - ○ Quantitative RT-PCR
  - ○ ChIP-seq Assays
  - ○ ChIP-seq Analysis
  - ○ ChromHMM Transition
  - ○ Glucose Uptake and Lactate Excretion Assay
  - ○ Metabolomics Experiments
  - ○ Inhibitor Experiments
  - ○ Extracellular Flux Assays Using Seahorse Analyzer
  - ○ Three-Dimensional Cell Culture
  - ○ *In Vivo* Inhibitor Experiments
  - ○ Stable Knockdown, Overexpression, and Rescue Experiments
  - ○ Measurement of GAPDH and Enolase Activities
- ● QUANTIFICATION AND STATISTICAL ANALYSIS
- ● DATA AND CODE AVAILABILTY

SUPPLEMENTAL INFORMATION

Supplemental Information can be found online at https://doi.org/10.1016/j.ccell.2020.03.005.

ACKNOWLEDGMENTS

We are grateful to Julien Sage, Joseph R. Marszalek, and Laura Pasqualucci for providing their reagents and thank Haoqiang Ying for insightful discussion. We are also thankful to Kathryn Hale (Scientific Publications Services, Research Medical Library, The University of Texas MD Anderson Cancer Center) for the editorial assistance and to Zhenbo Han, Su Zhang, and Charles Kingsley for their technical assistance. This work was supported by grants to M.G.L. from the National Institutes of Health (NIH; R01CA157919, R01CA207109, and R01CA207098) and the Center for Cancer Epigenetics (Solexa allowance) at the MD Anderson Cancer Center, by a grant to K.R. from the NIH (R00CA160578), by a grant to F.L.M. from American Cancer Society (RSG-15-145-01-CDD), by a grant to F.J.D. from the Intramural Research Program of the National Institute of Environmental Health Sciences (Z1AES103311-10), by a grant to E.R.F. from the NIH (R35CA197452), by grants to N.P. from the Cancer Prevention and Research Institute of Texas (The Proteomics and Metabolomics Core Facility, RP170005), the American Cancer Society (127430-RSG-15-105-01-CNE), and the NIH (R01CA216426 and R01CA220297), by a fellowship to M.K. from the Center for Cancer Epigenetics at the MD Anderson Cancer Center, and by a fellowship to H.A. from the Odyssey program at the MD Anderson Cancer Center. The animal imaging and histology work were performed at the Small Animal Imaging Facility and Histopathology Core Lab, respectively, at the MD Anderson Cancer Center, supported by the NIH National Cancer Institute (P30CA016672).

AUTHOR CONTRIBUTIONS

H.A. planned and carried out a majority of experiments, analyzed data, prepared figures, and wrote the manuscript. M.T. performed the bioinformatics analysis of RNA-seq and ChIP-seq data, prepared bioinformatics figures, and wrote the manuscript. M.M. performed ChIP-seq experiments. S.S.D. performed ChIP and rescue experiments. M.K. performed cell death and enzyme assays. C.Y.H. prepared reagents and performed Seahorse experiments and data analysis. S.B.A. contributed to data analysis. T-Y.C. contributed to inhibitor experiments. B.G. helped animal experiments. J.C. contributed to IHC experiments and analysis. C.R.A.and N.P. analyzed metabolite data. Y.-H.L., F.L.M., E.R.F., and F.J.D. provided reagents. L.B. analyzed tumor data. K.R. directed ChIP-seq experiments, guided the bioinformatics study, contributed to experiment design, and wrote the manuscript. M.G.L. conceived the study, designed and oversaw the study, evaluated data, and wrote the manuscript.

DECLARATION OF INTERESTS

The authors declare no competing interests.

Received: March 29, 2019
Revised: November 8, 2019
Accepted: March 4, 2020
Published: April 2, 2020

REFERENCES

Alam, H., Li, N., Dhar, S.S., Wu, S.J., Lv, J., Chen, K., Flores, E.R., Baseler, L., and Lee, M.G. (2018). HP1gamma promotes lung adenocarcinoma by downregulating the transcription-repressive regulators NCOR2 and ZBTB7A. Cancer Res. *78*, 3834–3848.

Barski, A., Cuddapah, S., Cui, K., Roh, T.Y., Schones, D.E., Wang, Z., Wei, G., Chepelev, I., and Zhao, K. (2007). High-resolution profiling of histone methylations in the human genome. Cell *129*, 823–837.

Bass, J., and Takahashi, J.S. (2010). Circadian integration of metabolism and energetics. Science *330*, 1349–1354.

Bjornsson, H.T., Benjamin, J.S., Zhang, L., Weissman, J., Gerber, E.E., Chen, Y.C., Vaurio, R.G., Potter, M.C., Hansen, K.D., and Dietz, H.C. (2014). Histone deacetylase inhibition rescues structural and functional brain deficits in a mouse model of Kabuki syndrome. Sci. Transl. Med. *6*, 256ra135.

Brawer, M.K. (2005). Lonidamine: basic science and rationale for treatment of prostatic proliferative disorders. Rev. Urol. *7* (*Suppl 7*), S21–S26.

Campbell, J.D., Alexandrov, A., Kim, J., Wala, J., Berger, A.H., Pedamallu, C.S., Shukla, S.A., Guo, G., Brooks, A.N., Murray, B.A., et al. (2016). Distinct patterns of somatic genome alterations in lung adenocarcinomas and squamous cell carcinomas. Nat. Genet. *48*, 607–616.

Cancer Genome Atlas Research Network (2012). Comprehensive genomic characterization of squamous cell lung cancers. Nature *489*, 519–525.

Cancer Genome Atlas Research Network (2014). Comprehensive molecular profiling of lung adenocarcinoma. Nature *511*, 543–550.

(B) The effect of KMT2D knockdown on glucose uptake (left panel) and lactate excretion (right panel) in LKR10 cells.

(C and D) Rescue experiments by ectopic expression of a functional but smaller KMT2D protein in LKR10 cells. KMT2D-depleted LKR10 cells were transfected with pFLAG-CMV2 expression plasmids encoding mini-KMT2D. Expression of glycolytic genes (C) as well as eRNA levels for two different regions (E1 and E2) of *Per2* (D, top panels) were analyzed using qRT-PCR. H3K27ac levels were analyzed by quantitative ChIP (D, bottom panels).

(E and F) Effect of Dox-induced *KMT2D* on glucose uptake (E, top panel) and lactate excretion (E, bottom panel) in H1568 cells and on expression of glycolytic genes (F). H1568 cells bearing Dox-inducible *KMT2D* were treated with 10 μg/mL Dox.

(G) Analysis of the effect of exogenous *PER2* expression on *Eno1*, *Pgk1*, *Pgam1*, *Ldha*, *Gapdh*, and *Cdk1* mRNA levels in LKR-10 cells using qRT-PCR.

(H) Analysis of the effect of PER2 knockdown on *Eno1*, *Pgk1*, *Pgam1*, *Ldha*, *Gapdh*, and *Cdk1* mRNA levels in LKR-10 cells using qRT-PCR.

(I) Scatterplots showing inverse correlations of *PER2* mRNA levels with *ENO1*, *PGK1*, *PGAM1*, *LDHA*, or *CDK1 mRNA* levels in human LUADs in the TCGA dataset (n = 517). r, Pearson's correlation coefficient.

In (A) to (H), data are presented as the mean ± SEM (error bars) of at least three independent experiments or biological replicates. $^{*}p < 0.05$, $^{**}p < 0.01$, $^{***}p < 0.001$ (two-tailed Student's t test). See also Figure S8.

Capello, M., Ferri-Borgogno, S., Cappello, P., and Novelli, F. (2011). alpha-Enolase: a promising therapeutic and diagnostic tumor target. FEBS J. *278*, 1064–1074.

Cerami, E., Gao, J., Dogrusoz, U., Gross, B.E., Sumer, S.O., Aksoy, B.A., Jacobsen, A., Byrne, C.J., Heuer, M.L., Larsson, E., et al. (2012). The cBio cancer genomics portal: an open platform for exploring multidimensional cancer genomics data. Cancer Discov. *2*, 401–404.

Chan, B.A., and Hughes, B.G. (2015). Targeted therapy for non-small cell lung cancer: current standards and the promise of the future. Transl. Lung Cancer Res. *4*, 36–54.

Cho, Y.W., Hong, T., Hong, S., Guo, H., Yu, H., Kim, D., Guszczynski, T., Dressler, G.R., Copeland, T.D., Kalkum, M., et al. (2007). PTIP associates with MLL3- and MLL4-containing histone H3 lysine 4 methyltransferase complex. J. Biol. Chem. *282*, 20395–20406.

Colaprico, A., Silva, T.C., Olsen, C., Garofano, L., Cava, C., Garolini, D., Sabedot, T.S., Malta, T.M., Pagnotta, S.M., Castiglioni, I., et al. (2016). TCGAbiolinks: an R/Bioconductor package for integrative analysis of TCGA data. Nucleic Acids Res. *44*, e71.

Colell, A., Green, D.R., and Ricci, J.E. (2009). Novel roles for GAPDH in cell death and carcinogenesis. Cell Death Differ. *16*, 1573–1581.

Dawson, M.A., and Kouzarides, T. (2012). Cancer epigenetics: from mechanism to therapy. Cell *150*, 12–27.

Dhar, S.S., Lee, S.H., Kan, P.Y., Voigt, P., Ma, L., Shi, X., Reinberg, D., and Lee, M.G. (2012). Trans-tail regulation of MLL4-catalyzed H3K4 methylation by H4R3 symmetric dimethylation is mediated by a tandem PHD of MLL4. Genes Dev. *26*, 2749–2762.

Dhar, S.S., Zhao, D., Lin, T., Gu, B., Pal, K., Wu, S.J., Alam, H., Lv, J., Yun, K., Gopalakrishnan, V., et al. (2018). MLL4 is required to maintain broad H3K4me3 peaks and super-enhancers at tumor suppressor genes. Mol. Cell *70*, 825–841 e826.

Dobin, A., Davis, C.A., Schlesinger, F., Drenkow, J., Zaleski, C., Jha, S., Batut, P., Chaisson, M., and Gingeras, T.R. (2013). STAR: ultrafast universal RNA-seq aligner. Bioinformatics *29*, 15–21.

Donehower, L.A., Harvey, M., Slagle, B.L., McArthur, M.J., Montgomery, C.A., Jr., Butel, J.S., and Bradley, A. (1992). Mice deficient for p53 are developmentally normal but susceptible to spontaneous tumours. Nature *356*, 215–221.

Dorighi, K.M., Swigut, T., Henriques, T., Bhanu, N.V., Scruggs, B.S., Nady, N., Still, C.D., 2nd, Garcia, B.A., Adelman, K., and Wysocka, J. (2017). Mll3 and Mll4 Facilitate Enhancer RNA Synthesis and Transcription from Promoters Independently of H3K4 Monomethylation. Mol. Cell *66*, 568–576.e564.

DuPage, M., Dooley, A.L., and Jacks, T. (2009). Conditional mouse lung cancer models using adenoviral or lentiviral delivery of Cre recombinase. Nat. Protoc. *4*, 1064–1072.

Ernst, J., and Kellis, M. (2012). ChromHMM: automating chromatin-state discovery and characterization. Nat. Methods *9*, 215–216.

Filipski, E., King, V.M., Li, X., Granda, T.G., Mormont, M.C., Claustrat, B., Hastings, M.H., and Levi, F. (2003). Disruption of circadian coordination accelerates malignant growth in mice. Pathol. Biol. (Paris) *51*, 216–219.

Fu, L., Pelicano, H., Liu, J., Huang, P., and Lee, C. (2002). The circadian gene Period2 plays an important role in tumor suppression and DNA damage response in vivo. Cell *111*, 41–50.

Ganapathy-Kanniappan, S., Kunjithapatham, R., and Geschwind, J.F. (2013). Anticancer efficacy of the metabolic blocker 3-bromopyruvate: specific molecular targeting. Anticancer Res. *33*, 13–20.

Gao, J., Aksoy, B.A., Dogrusoz, U., Dresdner, G., Gross, B., Sumer, S.O., Sun, Y., Jacobsen, A., Sinha, R., Larsson, E., et al. (2013). Integrative analysis of complex cancer genomics and clinical profiles using the cBioPortal. Sci. Signal. *6*, pl1.

Gatenby, R.A., and Gillies, R.J. (2004). Why do cancers have high aerobic glycolysis? Nat. Rev. Cancer *4*, 891–899.

Gel, B., and Serra, E. (2017). karyoploteR: an R/Bioconductor package to plot customizable genomes displaying arbitrary data. Bioinformatics *33*, 3088–3090.

Gu, Z., Eils, R., and Schlesner, M. (2016). Complex heatmaps reveal patterns and correlations in multidimensional genomic data. Bioinformatics *32*, 2847–2849.

Gu, Z., Eils, R., Schlesner, M., and Ishaque, N. (2018). EnrichedHeatmap: an R/Bioconductor package for comprehensive visualization of genomic signal associations. BMC Genomics *19*, 234.

Gyorffy, B., Surowiak, P., Budczies, J., and Lanczky, A. (2013). Online survival analysis software to assess the prognostic value of biomarkers using transcriptomic data in non-small-cell lung cancer. PLoS One *8*, e82241.

Hawkins, R.D., Hon, G.C., Lee, L.K., Ngo, Q., Lister, R., Pelizzola, M., Edsall, L.E., Kuan, S., Luu, Y., Klugman, S., et al. (2010). Distinct epigenomic landscapes of pluripotent and lineage-committed human cells. Cell Stem Cell *6*, 479–491.

Herbst, R.S., Heymach, J.V., and Lippman, S.M. (2008). Lung cancer. N. Engl. J. Med. *359*, 1367–1380.

Herbst, R.S., Morgensztern, D., and Boshoff, C. (2018). The biology and management of non-small cell lung cancer. Nature *553*, 446–454.

Herz, H.M., Mohan, M., Garruss, A.S., Liang, K., Takahashi, Y.H., Mickey, K., Voets, O., Verrijzer, C.P., and Shilatifard, A. (2012). Enhancer-associated H3K4 monomethylation by Trithorax-related, the Drosophila homolog of mammalian Mll3/Mll4. Genes Dev. *26*, 2604–2620.

Hitosugi, T., Zhou, L., Elf, S., Fan, J., Kang, H.B., Seo, J.H., Shan, C., Dai, Q., Zhang, L., Xie, J., et al. (2012). Phosphoglycerate mutase 1 coordinates glycolysis and biosynthesis to promote tumor growth. Cancer Cell *22*, 585–600.

Huang, C.C., Wang, S.Y., Lin, L.L., Wang, P.W., Chen, T.Y., Hsu, W.M., Lin, T.K., Liou, C.W., and Chuang, J.H. (2015). Glycolytic inhibitor 2-deoxyglucose simultaneously targets cancer and endothelial cells to suppress neuroblastoma growth in mice. Dis. Model. Mech. *8*, 1247–1254.

Imielinski, M., Berger, A.H., Hammerman, P.S., Hernandez, B., Pugh, T.J., Hodis, E., Cho, J., Suh, J., Capelletti, M., Sivachenko, A., et al. (2012). Mapping the hallmarks of lung adenocarcinoma with massively parallel sequencing. Cell *150*, 1107–1120.

Issaeva, I., Zonis, Y., Rozovskaia, T., Orlovsky, K., Croce, C.M., Nakamura, T., Mazo, A., Eisenbach, L., and Canaani, E. (2007). Knockdown of ALR (MLL2) reveals ALR target genes and leads to alterations in cell adhesion and growth. Mol. Cell. Biol. *27*, 1889–1903.

Jackson, E.L., Willis, N., Mercer, K., Bronson, R.T., Crowley, D., Montoya, R., Jacks, T., and Tuveson, D.A. (2001). Analysis of lung tumor initiation and progression using conditional expression of oncogenic K-ras. Genes Dev. *15*, 3243–3248.

Jacob, A., Oblinger, J., Bush, M.L., Brendel, V., Santarelli, G., Chaudhury, A.R., Kulp, S., La Perle, K.M., Chen, C.S., Chang, L.S., et al. (2012). Preclinical validation of AR42, a novel histone deacetylase inhibitor, as treatment for vestibular schwannomas. Laryngoscope *122*, 174–189.

Jang, Y., Broun, A., Wang, C., Park, Y.K., Zhuang, L., Lee, J.E., Froimchuk, E., Liu, C., and Ge, K. (2019). H3.3K4M destabilizes enhancer H3K4 methyltransferases MLL3/MLL4 and impairs adipose tissue development. Nucleic Acids Res. *47*, 607–620.

Kandoth, C., McLellan, M.D., Vandin, F., Ye, K., Niu, B., Lu, C., Xie, M., Zhang, Q., McMichael, J.F., Wyczalkowski, M.A., et al. (2013). Mutational landscape and significance across 12 major cancer types. Nature *502*, 333–339.

Kim, T.K., and Shiekhattar, R. (2015). Architectural and functional commonalities between enhancers and promoters. Cell *162*, 948–959.

Koike, N., Yoo, S.H., Huang, H.C., Kumar, V., Lee, C., Kim, T.K., and Takahashi, J.S. (2012). Transcriptional architecture and chromatin landscape of the core circadian clock in mammals. Science *338*, 349–354.

Koster, J., and Rahmann, S. (2012). Snakemake—a scalable bioinformatics workflow engine. Bioinformatics *28*, 2520–2522.

Koutsioumpa, M., Hatziapostolou, M., Polytarchou, C., Tolosa, E.J., Almada, L.L., Mahurkar-Joshi, S., Williams, J., Tirado-Rodriguez, A.B., Huerta-Yepez, S., Karavias, D., et al. (2019). Lysine methyltransferase 2D regulates pancreatic carcinogenesis through metabolic reprogramming. Gut *68*, 1271–1286.

Lai, B., Lee, J.E., Jang, Y., Wang, L., Peng, W., and Ge, K. (2017). MLL3/MLL4 are required for CBP/p300 binding on enhancers and super-enhancer formation in brown adipogenesis. Nucleic Acids Res. *45*, 6388–6403.

Lang, G.A., Iwakuma, T., Suh, Y.A., Liu, G., Rao, V.A., Parant, J.M., Valentin-Vega, Y.A., Terzian, T., Caldwell, L.C., Strong, L.C., et al. (2004). Gain of function of a p53 hot spot mutation in a mouse model of Li-Fraumeni syndrome. Cell *119*, 861–872.

Langmead, B., Trapnell, C., Pop, M., and Salzberg, S.L. (2009). Ultrafast and memory-efficient alignment of short DNA sequences to the human genome. Genome Biol. *10*, R25.

Lee, G.Y., Kenny, P.A., Lee, E.H., and Bissell, M.J. (2007a). Three-dimensional culture models of normal and malignant breast epithelial cells. Nat. Methods *4*, 359–365.

Lee, J., Kim, D.H., Lee, S., Yang, Q.H., Lee, D.K., Lee, S.K., Roeder, R.G., and Lee, J.W. (2009). A tumor suppressive coactivator complex of p53 containing ASC-2 and histone H3-lysine-4 methyltransferase MLL3 or its paralogue MLL4. Proc. Natl. Acad. Sci. U S A *106*, 8513–8518.

Lee, J.E., Wang, C., Xu, S., Cho, Y.W., Wang, L., Feng, X., Baldridge, A., Sartorelli, V., Zhuang, L., Peng, W., et al. (2013). H3K4 mono- and di-methyltransferase MLL4 is required for enhancer activation during cell differentiation. Elife *2*, e01503.

Lee, M.G., Villa, R., Trojer, P., Norman, J., Yan, K.P., Reinberg, D., Di Croce, L., and Shiekhattar, R. (2007b). Demethylation of H3K27 regulates polycomb recruitment and H2A ubiquitination. Science *318*, 447–450.

Li, H., Handsaker, B., Wysoker, A., Fennell, T., Ruan, J., Homer, N., Marth, G., Abecasis, G., Durbin, R., and Genome Project Data Processing, S. (2009). The sequence alignment/map format and SAMtools. Bioinformatics *25*, 2078–2079.

Li, X., Jiang, Y., Meisenhelder, J., Yang, W., Hawke, D.H., Zheng, Y., Xia, Y., Aldape, K., He, J., Hunter, T., et al. (2016). Mitochondria-translocated PGK1 functions as a protein kinase to coordinate glycolysis and the TCA cycle in tumorigenesis. Mol. Cell *61*, 705–719.

Liao, Y., Smyth, G.K., and Shi, W. (2014). featureCounts: an efficient general purpose program for assigning sequence reads to genomic features. Bioinformatics *30*, 923–930.

Liberti, M.V., Dai, Z., Wardell, S.E., Baccile, J.A., Liu, X., Gao, X., Baldi, R., Mehrmohamadi, M., Johnson, M.O., Madhukar, N.S., et al. (2017). A predictive model for selective targeting of the Warburg effect through GAPDH inhibition with a natural product. Cell Metab. *26*, 648–659.e8.

Lin, Y.H., Satani, N., Hammoudi, N., Ackroyd, J.J., Khadka, S., Yan, V.C., Georgiou, D.K., Sun, Y., Zielinski, R., Tran, T., et al. (2018). Eradication of ENO1-deleted glioblastoma through collateral lethality. bioRxiv, 331538, https://doi.org/10.1101/331538.

Love, M.I., Huber, W., and Anders, S. (2014). Moderated estimation of fold change and dispersion for RNA-seq data with DESeq2. Genome Biol. *15*, 550.

Loven, J., Hoke, H.A., Lin, C.Y., Lau, A., Orlando, D.A., Vakoc, C.R., Bradner, J.E., Lee, T.I., and Young, R.A. (2013). Selective inhibition of tumor oncogenes by disruption of super-enhancers. Cell *153*, 320–334.

Maitituoheti, M., Keung, E.Z., Tang, M., Yan, L., Alam, H., Han, G., Raman, A.T., Terranova, C.J., Sarkar, S., Orouji, E., et al. (2018). Enhancer reprogramming confers dependence on glycolysis and IGF signaling in KMT2D mutant melanoma. bioRxiv, 507327, https://doi.org/10.1101/507327.

Malhotra, J., Jabbour, S.K., and Aisner, J. (2017). Current state of immunotherapy for non-small cell lung cancer. Transl. Lung Cancer Res. *6*, 196–211.

Malumbres, M., and Barbacid, M. (2009). Cell cycle, CDKs and cancer: a changing paradigm. Nat. Rev. Cancer *9*, 153–166.

Marx, V. (2015). Visualizing epigenomic data. Nat. Methods *12*, 499–502.

Molina, J.R., Sun, Y., Protopopova, M., Gera, S., Bandi, M., Bristow, C., McAfoos, T., Morlacchi, P., Ackroyd, J., Agip, A.A., et al. (2018). An inhibitor of oxidative phosphorylation exploits cancer vulnerability. Nat. Med. *24*, 1036–1046.

Nguyen, A.T., and Zhang, Y. (2011). The diverse functions of Dot1 and H3K79 methylation. Genes Dev. *25*, 1345–1358.

Olive, K.P., Tuveson, D.A., Ruhe, Z.C., Yin, B., Willis, N.A., Bronson, R.T., Crowley, D., and Jacks, T. (2004). Mutant p53 gain of function in two mouse models of Li-Fraumeni syndrome. Cell *119*, 847–860.

Ortega-Molina, A., Boss, I.W., Canela, A., Pan, H., Jiang, Y., Zhao, C., Jiang, M., Hu, D., Agirre, X., Niesvizky, I., et al. (2015). The histone lysine methyltransferase KMT2D sustains a gene expression program that represses B cell lymphoma development. Nat. Med. *21*, 1199–1208.

Papagiannakopoulos, T., Bauer, M.R., Davidson, S.M., Heimann, M., Subbaraj, L., Bhutkar, A., Bartlebaugh, J., Vander Heiden, M.G., and Jacks, T. (2016). Circadian rhythm disruption promotes lung tumorigenesis. Cell Metab. *24*, 324–331.

Parry, D., Guzi, T., Shanahan, F., Davis, N., Prabhavalkar, D., Wiswell, D., Seghezzi, W., Paruch, K., Dwyer, M.P., Doll, R., et al. (2010). Dinaciclib (SCH 727965), a novel and potent cyclin-dependent kinase inhibitor. Mol. Cancer Ther. *9*, 2344–2353.

Pelicano, H., Martin, D.S., Xu, R.H., and Huang, P. (2006). Glycolysis inhibition for anticancer treatment. Oncogene *25*, 4633–4646.

Putluri, N., Maity, S., Kommagani, R., Creighton, C.J., Putluri, V., Chen, F., Nanda, S., Bhowmik, S.K., Terunuma, A., Dorsey, T., et al. (2014). Pathway-centric integrative analysis identifies RRM2 as a prognostic marker in breast cancer associated with poor survival and tamoxifen resistance. Neoplasia *16*, 390–402.

Putluri, N., Shojaie, A., Vasu, V.T., Nalluri, S., Vareed, S.K., Putluri, V., Vivekanandan-Giri, A., Byun, J., Pennathur, S., Sana, T.R., et al. (2011). Metabolomic profiling reveals a role for androgen in activating amino acid metabolism and methylation in prostate cancer cells. PLoS One *6*, e21417.

Ramirez, F., Ryan, D.P., Gruning, B., Bhardwaj, V., Kilpert, F., Richter, A.S., Heyne, S., Dundar, F., and Manke, T. (2016). deepTools2: a next generation web server for deep-sequencing data analysis. Nucleic Acids Res. *44*, W160–W165.

Robinson, J.T., Thorvaldsdottir, H., Winckler, W., Guttman, M., Lander, E.S., Getz, G., and Mesirov, J.P. (2011). Integrative genomics viewer. Nat. Biotechnol. *29*, 24–26.

Santo, L., Vallet, S., Hideshima, T., Cirstea, D., Ikeda, H., Pozzi, S., Patel, K., Okawa, Y., Gorgun, G., Perrone, G., et al. (2010). AT7519, A novel small molecule multi-cyclin-dependent kinase inhibitor, induces apoptosis in multiple myeloma via GSK-3beta activation and RNA polymerase II inhibition. Oncogene *29*, 2325–2336.

Santos, M.A., Faryabi, R.B., Ergen, A.V., Day, A.M., Malhowski, A., Canela, A., Onozawa, M., Lee, J.E., Callen, E., Gutierrez-Martinez, P., et al. (2014). DNA-damage-induced differentiation of leukaemic cells as an anti-cancer barrier. Nature *514*, 107–111.

Schneider, C.A., Rasband, W.S., and Eliceiri, K.W. (2012). NIH Image to ImageJ: 25 years of image analysis. Nat. Methods *9*, 671–675.

Sharma, S.V., Bell, D.W., Settleman, J., and Haber, D.A. (2007). Epidermal growth factor receptor mutations in lung cancer. Nat. Rev. Cancer *7*, 169–181.

Sheng, S.L., Liu, J.J., Dai, Y.H., Sun, X.G., Xiong, X.P., and Huang, G. (2012). Knockdown of lactate dehydrogenase A suppresses tumor growth and metastasis of human hepatocellular carcinoma. FEBS J. *279*, 3898–3910.

Shilatifard, A. (2012). The COMPASS family of histone H3K4 methylases: mechanisms of regulation in development and disease pathogenesis. Annu. Rev. Biochem. *81*, 65–95.

Smith, E., and Shilatifard, A. (2014). Enhancer biology and enhanceropathies. Nat. Struct. Mol. Biol. *21*, 210–219.

Subramanian, A., Tamayo, P., Mootha, V.K., Mukherjee, S., Ebert, B.L., Gillette, M.A., Paulovich, A., Pomeroy, S.L., Golub, T.R., Lander, E.S., et al. (2005). Gene set enrichment analysis: a knowledge-based approach for interpreting genome-wide expression profiles. Proc. Natl. Acad. Sci. U S A *102*, 15545–15550.

Sun, Y., Zhou, B., Mao, F., Xu, J., Miao, H., Zou, Z., Phuc Khoa, L.T., Jang, Y., Cai, S., Witkin, M., et al. (2018). HOXA9 reprograms the enhancer landscape to promote leukemogenesis. Cancer Cell *34*, 643–658.e5.

Sur, I., and Taipale, J. (2016). The role of enhancers in cancer. Nat. Rev. Cancer *16*, 483–493.

Suva, M.L., Riggi, N., and Bernstein, B.E. (2013). Epigenetic reprogramming in cancer. Science *339*, 1567–1570.

Terranova, C., Tang, M., Orouji, E., Maitituoheti, M., Raman, A., Amin, S., Liu, Z., and Rai, K. (2018). An integrated platform for genome-wide mapping of chromatin states using high-throughput ChIP-sequencing in tumor tissues. J. Vis. Exp. https://doi.org/10.3791/56972.

Wagner, K.W., Alam, H., Dhar, S.S., Giri, U., Li, N., Wei, Y., Giri, D., Cascone, T., Kim, J.H., Ye, Y., et al. (2013). KDM2A promotes lung tumorigenesis by epigenetically enhancing ERK1/2 signaling. J. Clin. Invest. *123*, 5231–5246.

Wang, S.P., Tang, Z., Chen, C.W., Shimada, M., Koche, R.P., Wang, L.H., Nakadai, T., Chramiec, A., Krivtsov, A.V., Armstrong, S.A., et al. (2017a). A UTX-MLL4-p300 transcriptional regulatory network coordinately shapes active enhancer landscapes for eliciting transcription. Mol. Cell *67*, 308–321.e6.

Wang, X.Q., Lo, C.M., Chen, L., Ngan, E.S., Xu, A., and Poon, R.Y. (2017b). CDK1-PDK1-PI3K/Akt signaling pathway regulates embryonic and induced pluripotency. Cell Death Differ. *24*, 38–48.

Wangler, M.F., Chao, Y.H., Bayat, V., Giagtzoglou, N., Shinde, A.B., Putluri, N., Coarfa, C., Donti, T., Graham, B.H., Faust, J.E., et al. (2017). Peroxisomal biogenesis is genetically and biochemically linked to carbohydrate metabolism in Drosophila and mouse. PLoS Genet. *13*, e1006825.

Whyte, W.A., Orlando, D.A., Hnisz, D., Abraham, B.J., Lin, C.Y., Kagey, M.H., Rahl, P.B., Lee, T.I., and Young, R.A. (2013). Master transcription factors and mediator establish super-enhancers at key cell identity genes. Cell *153*, 307–319.

Wickham, H. (2006). An implementation of the grammar of graphics in R: ggplot. Paper presented at the 2006 use R conference: Book of Abstracts.

Yu, G., Wang, L.G., and He, Q.Y. (2015). ChIPseeker: an R/Bioconductor package for ChIP peak annotation, comparison and visualization. Bioinformatics *31*, 2382–2383.

Zhang, D., Li, J., Wang, F., Hu, J., Wang, S., and Sun, Y. (2014). 2-Deoxy-D-glucose targeting of glucose metabolism in cancer cells as a potential therapy. Cancer Lett. *355*, 176–183.

Zhang, J., Dominguez-Sola, D., Hussein, S., Lee, J.E., Holmes, A.B., Bansal, M., Vlasevska, S., Mo, T., Tang, H., Basso, K., et al. (2015a). Disruption of KMT2D perturbs germinal center B cell development and promotes lymphomagenesis. Nat. Med. *21*, 1190–1198.

Zhang, Y., Liu, T., Meyer, C.A., Eeckhoute, J., Johnson, D.S., Bernstein, B.E., Nusbaum, C., Myers, R.M., Brown, M., Li, W., et al. (2008). Model-based analysis of ChIP-seq (MACS). Genome Biol. *9*, R137.

Zhang, Y., Mittal, A., Reid, J., Reich, S., Gamblin, S.J., and Wilson, J.R. (2015b). Evolving catalytic properties of the MLL family SET domain. Structure *23*, 1921–1933.

Please cite this article in press as: Alam et al., KMT2D Deficiency Impairs Super-Enhancers to Confer a Glycolytic Vulnerability in Lung Cancer, Cancer Cell (2020), https://doi.org/10.1016/j.ccell.2020.03.005

STAR★METHODS

KEY RESOURCES TABLE

REAGENT or RESOURCE	SOURCE	IDENTIFIER
Antibodies		
H3K27ac	Abcam	Cat# ab4729; RRID: AB_2118291
H3K27me3	Abcam	Cat# ab6002; RRID: AB_305237
H3K4me1	Cell Signaling Technology	Cat# 5326; RRID: AB_10695148
H3K4me3	Abcam	Cat# ab8580; RRID:AB_306649
H3	Abcam	Cat# ab1791; RRID:AB_302613
TTF-1	Seven Hills Bioreagents	Cat# WRAB-1231; RRID: AB_451727
Ki-67	Cell Signaling Technology	Cat# 9027; RRID: AB_2636984
ENO1	Abcam	Cat# ab227978
PGK1	Abcam	Cat# ab38007; RRID: AB_2161220
PGAM1	Novus	Cat# NBP1-49532; RRID: AB_10011581
TTF-1	Abcam	Cat# ab72876; RRID: AB_1271363
KMT2D	Santa Cruz Biotechnology	Cat# sc-68675; RRID: AB_2145784
Actin	Sigma-Aldrich	Cat# A5441; RRID: AB_476744
HRP-conjugated anti-mouse-IgG	Santa Cruz Biotechnology	Cat# sc-2055; RRID: AB_631738
HRP-conjugated anti-rabbit-IgG	Santa Cruz Biotechnology	Cat# sc-2004; RRID: AB_631746
Alexa 488-conjugated anti-mouse IgG	Life technologies	Cat# A-11029; RRID: AB_138404
Alexa 488-conjugated anti-rabbit IgG	Life technologies	Cat# A-11037; RRID: AB_2534095
Chemicals, Peptides, and Recombinant Proteins		
2-Deoxy-D-glucose (2-DG)	Selleck Chemicals	Cat# S4701; CAS: 1032350-13-2
Vorinostat (SAHA, MK0683)	Selleck Chemicals	Cat# S1047; CAS: 149647-78-9
AR-42 (HDAC-42)	Selleck Chemicals	Cat# S2244; CAS: 935881-37-1
Lonidamine	Selleck Chemicals	Cat# S2610; CAS: 50264-69-2
Dinaciclib	Selleck Chemicals	Cat# S2768; CAS: 779353-01-4
Koningic acid (KA)	Focus Biomolecule	Cat# 10-3326; CAS: 74310-84-2
IACS-010759	Gift from Dr. Joseph R. Marszalek (Molina et al., 2018)	N/A
Critical Commercial Assays		
Seahorse XF Glycolysis stress test kit	Agilent	Cat# 103020-100
Seahorse XF Cell Mito stress test kit	Agilent	Cat# 103015-100
Glyceraldehyde 3 Phosphate Dehydrogenase Activity Assay Kit	Abcam	Cat# ab204732
Enolase Assays Kit	Abcam	Cat# ab241024
Deposited Data		
RNA-seq for*Kras*$^{LSL\text{-}G12D}$ and *Kras*$^{LSL\text{-}G12D}$;*Kmt2d*$^{fl/fl}$ lung tumors	This paper	GEO: GSE116658
ChIP-seq for *Kras*$^{LSL\text{-}G12D}$ and *Kras*$^{LSL\text{-}G12D}$;*Kmt2d*$^{fl/fl}$ lung tumors	This paper	GEO: GSE116659
RNA-seq for LKR10 lung cancer cell line	This paper	GEO: GSE143498
Experimental Models: Cell Lines		
Human: NCI-A549	ATCC	CCL-185
Human: NCI-H1792	ATCC	CRL-5895
Human: NCI-H23	ATCC	CRL-5800
Human: NCI-H1437	ATCC	CRL-5872
Human: NCI-H358	ATCC	CRL-5807

(*Continued on next page*)

Continued

REAGENT or RESOURCE	SOURCE	IDENTIFIER
Human: NCI-H1568	ATCC	CRL-5876
Human: DV-90	DSMZ	ACC 307
Human: CORL-105	ECACC	92031918
Mouse: LKR-10	Gift from Julien Sage	N/A
Experimental Models: Organisms/Strains		
Mouse: B6.129-Krastm4Tyj/Nci,	NCI Mouse Repository	Strain: 01XJ6
Mouse: B6.129P2-*Trp53*^{tm1Brn}/J	The Jackson Laboratory	Strain: 008462
Mouse: *Kmt2d*$^{fl/fl}$ (also called *Mll4*$^{fl/fl}$)	(Dhar et al., 2018)	N/A
Oligonucleotides		
Primers for quantitative RT-PCR (mouse): See Table S4	N/A	N/A
Primers for quantitative RT-PCR for enhancer RNAs: See Table S4	N/A	N/A
Primers for genotyping: See Table S4	N/A	N/A
Primers for quantitative ChIP-PCR (mouse): See Table S4	N/A	N/A
Primers for cloning: See Table S4	N/A	N/A
Recombinant DNA		
pInducer20-*KMT2D*	This paper	N/A
sh*Kmt2d*-01 (mouse)	Sigma-Aldrich	Cat# TRCN0000239234
sh*Kmt2d*-03 (mouse)	Sigma-Aldrich	Cat# TRCN0000239233
sh*Per2*-01 (mouse)	Sigma-Aldrich	Cat# TRCN0000284505
sh*Per2*-02(mouse)	Sigma-Aldrich	Cat# TRCN0000096663
Software and Algorithms		
ImageJ	(Schneider et al., 2012)	https://imagej.nih.gov/ij/
cBio cancer genomics portal	(Cerami et al., 2012; Gao et al., 2013)	http://www.cbioportal.org/
IBM SPSS Statistics 23	IBM	https://www.ibm.com/support/pages/downloading-ibm-spss-statistics-23
Pyflow-ChIPseq	(Terranova et al., 2018)	https://github.com/crazyhottommy/pyflow-ChIPseq
Bowtie1	(Langmead et al., 2009)	http://bowtie-bio.sourceforge.net/index.shtml
samtools	(Li et al., 2009)	http://www.htslib.org/
Deeptools	(Ramirez et al., 2016)	https://deeptools.readthedocs.io/
MACS14	(Zhang et al., 2008)	https://github.com/taoliu/MACS
ROSE	(Whyte et al., 2013)	http://younglab.wi.mit.edu/super_enhancer_code.html
chromHMM	(Ernst and Kellis, 2012)	http://compbio.mit.edu/ChromHMM/
Epilogos	(Marx, 2015)	https://github.com/Altius/epilogos
EnrichedHeatmap	(Gu et al., 2018)	https://bioconductor.org/packages/release/bioc/html/EnrichedHeatmap.html
ComplexHeatmap	(Gu et al., 2016)	https://bioconductor.org/packages/release/bioc/html/ComplexHeatmap.html
STAR	(Dobin et al., 2013)	https://github.com/alexdobin/STAR
featureCounts	(Liao et al., 2014)	http://subread.sourceforge.net/
ChIPseeker	(Yu et al., 2015)	https://bioconductor.org/packages/release/bioc/html/ChIPseeker.html
DESeq2	(Love et al., 2014)	http://bioconductor.org/packages/release/bioc/html/DESeq2.html

(*Continued on next page*)

Please cite this article in press as: Alam et al., KMT2D Deficiency Impairs Super-Enhancers to Confer a Glycolytic Vulnerability in Lung Cancer, Cancer Cell (2020), https://doi.org/10.1016/j.ccell.2020.03.005

Continued

REAGENT or RESOURCE	SOURCE	IDENTIFIER
TCGAbiolinks	(Colaprico et al., 2016)	https://bioconductor.org/packages/release/bioc/html/TCGAbiolinks.html
KaryoploteR	(Gel and Serra, 2017)	http://bioconductor.org/packages/release/bioc/html/karyoploteR.html
GSEA	(Subramanian et al., 2005)	http://software.broadinstitute.org/gsea/
Snakemake	(Koster and Rahmann, 2012)	https://snakemake.readthedocs.io/en/stable/
Pyflow-RNAseq	This paper	https://github.com/crazyhottommy/pyflow-RNAseq
IGV	(Robinson et al., 2011)	https://software.broadinstitute.org/software/igv/
ggplot2	(Wickham, 2006)	https://ggplot2.tidyverse.org/

LEAD CONTACT AND MATERIALS AVAILABILITY

Requests for further information and reagents should be directed to and will be fulfilled by the Lead Contact, Min Gyu Lee (mglee@mdanderson.org). Any plasmid and cell line generated in this study would be available upon request.

EXPERIMENTAL MODEL AND SUBJECT DETAILS

Cell Lines

All lung cancer cell lines (A549, H1792, H23, H1437, H358, H1568, DV-90, CORL-105, and LKR-10) that were used in this study are described in the Key Resources Table, and they were cultured within 10 to 15 passages. Cell culture reagents and other chemicals were purchased from Thermo Fisher Scientific (Gibco & Hyclone), Corning, Sigma-Aldrich, and Fisher Bioreagents.

Mouse Strains and Genetically Engineered Lung Cancer Mouse Models

The *Kras*$^{LSL\text{-}G12D}$ (strain number 01XJ6) and *Trp53*$^{fl/fl}$ (strain name, B6.129P2-*Trp53*^{tm1Brn}/J; stock number, 008462) mice were obtained from the NCI Mouse Repository and Jackson Laboratory, respectively. The *Kmt2d*$^{fl/fl}$ mice were previously described (Dhar et al., 2018). *Kmt2d*$^{fl/fl}$ mice were crossed with *Kras*$^{LSL\text{-}G12D}$ or *Trp53*$^{fl/fl}$ mice to get the desired mouse genotypes of the study. To generate *Kras*$^{LSL\text{-}G12D}$;*Kmt2d*$^{fl/fl}$ mice, *Kmt2d*$^{fl/fl}$ mice were first crossed with *Kras*$^{LSL\text{-}G12D}$ mice and the resulting *Kras*$^{LSL\text{-}G12D}$;*Kmt2d*$^{fl/+}$ mice were then crossed with *Kmt2d*$^{fl/fl}$ mice. To generate *Trp53*$^{fl/fl}$;*Kmt2d*$^{fl/fl}$ mice, *Kmt2d*$^{fl/fl}$ were first crossed with *Trp53*$^{fl/fl}$, and the resulting *Trp53*$^{fl/+}$;*Kmt2d*$^{fl/+}$ mice were then crossed with *Trp53*$^{fl/+}$;*Kmt2d*$^{fl/+}$ to get *Trp53*$^{fl/fl}$;*Kmt2d*$^{fl/fl}$ mice. The genotypes of these mice were confirmed by a standard PCR-based protocol. The primers used for the genotyping are listed in Table S4.

In Vivo Lung Tumorigenesis Study

The protocol for induction and monitoring of lung tumorigenesis was described previously (Alam et al., 2018). In brief, to induce tumors in the mouse lung, 6- to 8-week old mice were infected with about 2.5×10^7 adeno 5 (Ad5)-CMV-Cre virus per mouse by the intratracheal intubation method (DuPage et al., 2009). The tumor progression and survival of mouse groups were compared. For chromatin immunoprecipitation (ChIP) and RNA analyses, the distinct tumors were dissected from the lungs, washed with ice-cold phosphate-buffered saline solution (PBS) and snap frozen. For histology, immunohistochemistry (IHC), and immunofluorescence (IF) analyses, tumor-bearing lungs were isolated, fixed and processed as previously described (Wagner et al., 2013). Hematoxylin and eosin (H&E)-stained sections of tumor-bearing lungs were evaluated microscopically, and tumors were scored 0, I, II, III, and IV on the basis of percentage of pulmonary parenchyma affected by lung adenocarcinoma(s): 0, no tumor present; I, <10% of examined lung affected; II, 10%–20%; III, 21%–50%; IV, >50%. Tumor areas were quantified using ImageScope software.

Study Approval

The care and use of all mice were approved by the Institutional Animal Care and Use Committee (IACUC) of The University of Texas MD Anderson Cancer Center.

METHOD DETAILS

Micro-Computed Tomography

Tumor growth in mice was monitored by using micro-CT as previously described (Alam et al., 2018). Briefly, the mice were anesthetized with 5% isoflurane and maintained at 2% isoflurane. The mice were intubated using a 20 gauge x 1-inch catheter and were transferred onto the bed of X-Rad 225Cx (Precision X-Ray Corporation). The mice were mechanically ventilated in a small animal ventilator, and micro-CT images were captured at 60 KvP, 4 mA, and 3 rpm. Each animal's breathing was held at 20cm$H_2$0 during the 20-second acquisition. Three to five mice (30 days post-infection) per group were subjected to micro-CT.

Histologic, Immunohistochemical, and Immunofluorescence Analyses

The tumor-bearing lungs were isolated and fixed with 10% formalin buffer. The fixed lung tissues were embedded in paraffin and were cut into 8 μm sections. For histologic examination, a standard H&E staining was performed. IHC and IF experiments were performed as described previously (Alam et al., 2018). Briefly, sections were subjected to antigen retrieval in a solution from Vector Laboratories (Burlingame, CA) and then blocked in 10% horse serum for 1 hr at RT. For IF, anti-mouse IgG antibodies conjugated to Alexa Fluor 488 and anti-rabbit IgG secondary antibodies conjugated to Alexa 568 were used for detection, and images of tumor regions were captured using a laser confocal microscope. For the quantification of IF staining, signal intensities of glycolytic enzymes in TTF1-positive tumor cells were measured using ImageJ software. The primary antibodies used for IHC are listed in the Key Resources Table.

Survival Analysis and Gene Expression Correlation Analysis

The LUAD datasets of TCGA database were used for expression and survival analysis. Oncoprint and correlation data were obtained by analysis using the cBioportal for cancer genomics (http://www.cbioportal.org) (Cancer Genome Atlas Research, 2014; Cerami et al., 2012; Gao et al., 2013). For the survival analysis, a publicly available LUAD transcriptomic dataset (http://kmplot.com/analysis/index.php?p=service&cancer=lung) (Gyorffy et al., 2013) was also used.

RNA Isolation from Lung Tumor Cells

The distinct tumor tissues were dissected and cut into < 1-mm pieces. The dissected tumor tissues were then digested in collagenase type 1 and DNAase I for 45 min and treated with 0.25% trypsin for 10 min. To remove red blood cells, the digested single cell suspension was treated with red blood cell lysis buffer for 2–3 min. To further enrich tumor cells, CD45-positive cells were removed using MagniSort™ Mouse CD45 Depletion Kit (ThermoFisher Scientific). The depletion of CD45-positive cells was confirmed by flow cytometry analysis. Total RNA was isolated using Trizol reagent (Life Technologies).

RNA-seq Analysis

The RNAs isolated from CD45-depleted tumor tissue samples were sequenced using the Illumina HiSeq 2000. The RNAs for shLuc-treated and KMT2D-depleted LKR10 lung cancer cells were sequenced using NextSeq 500. Both RNAseq data sets were processed by pyflow-RNAseq (https://github.com/crazyhottommy/pyflow-RNAseq), a Snakemake-based RNAseq pipeline. Raw reads were mapped by STAR (Dobin et al., 2013), RPKM normalized bigwigs were generated by deeptools (Ramirez et al., 2016), and gene counts were obtained by featureCounts (Liao et al., 2014). Differential expression analysis was carried out using DESeq2 (Love et al., 2014). DAVID (version 6.8) was used for gene ontology analysis. Gene Set Enrichment Analysis was carried out using the GSEA tool from the Broad Institute (Subramanian et al., 2005). The pre-rank mode was used. The signed fold change $*-\log_{10}$ (p value) metric was used for pre-ranking the genes.

TCGA RNA-seq Data Analysis

RNA-seq raw counts for TCGA lung adenocarcinoma dataset were downloaded using TCGAbiolinks (Colaprico et al., 2016). The mutation MAF files were downloaded with TCGAbiolinks as well, and mutation status was inferred from the MAF files. Twenty four LUAD samples with high WT *KMT2D* expression were compared with twenty LUAD samples with low WT *KMT2D* expression and four LUAD samples with *KMT2D* nonsense mutations using DESeq2 (see Table S2 for sample IDs). The signed fold change $*-\log_{10}$ (p value) metric was used to pre-rank the gene list in GSEA pre-rank analysis.

Quantitative RT-PCR

Quantitative reverse transcription (RT)-PCR analyses were performed as described earlier (Alam et al., 2018). In brief, iQ SYBR Green Supermix (BioRad) was used for PCR amplification, and signals were acquired using CFX384 Touch^{TM} real-time PCR detection system (BioRad). β-Actin mRNA or 18s rRNA levels were used for data normalization. Each experiment was performed in triplicate. The primers used for quantitative RT-PCR are listed in the Table S4.

ChIP-seq Assays

ChIP for lung tumor tissues was performed with minor modifications of a previous procedure (Terranova et al., 2018). Briefly, distinct lung tumor tissues (3 mg per antibody) were dissected from the lungs, cut into 1-mm pieces, homogenized using a MACS dissociator, and cross-linked using 1% paraformaldehyde for 10 min at 37°C. Crosslinking was then stopped by adding 0.125 M glycine for 5 min, and tissues were washed with PBS and stored at -80°C. Later, tissues were thawed on ice and lysed with ChIP harvest buffer (12 mM Tris-HCl, 0.1 × PBS, 6 mM EDTA, 0.5% sodium dodecyl sulfate [SDS]) for 10 min on ice. Sonication conditions were optimized for lung tumor tissues using bioruptor sonicator to achieve a shear length of 250–500 bp. Antibody-dynabead mixtures were incubated for 1 hr at 4°C and tissue extracts were then incubated overnight with these mixtures. After overnight incubation, immunecomplexes were washed as follows: five times with RIPA buffer, twice with RIPA-500 (RIPA with 500 mM NaCl) and twice with LiCl wash buffer

(10 mM Tris-HCl pH8.0, 1 mM EDTA pH8.0, 250 mM LiCl, 0.5% NP-40, 0.1% deoxycholate). For reverse-crosslinking and elution, immunecomplexes were incubated overnight at 65°C in elution buffer (10 mM Tris-HCl pH8.0, 5 mM EDTA, 300 mM NaCl, 0.5% SDS). Eluted DNA was then treated with proteinase K (20 mg/ml) and RNaseA and DNA clean-up was done using SPRI beads (Beckman-Coulter). Libraries were prepared as previously described (Terranova et al., 2018) using adaptors from New England Biolabs. Libraries were multiplexed together and sequenced in HiSeq2000 or HiSeq4000 (Illumina).

ChIP-seq Analysis

ChIP-seq data that were generated using *Kras* and *Kras*;*Kmt2d*$^{-/-}$ tumors were quality-controlled and processed by pyflow-ChIPseq (Terranova et al., 2018), a Snakemake-based ChIP-seq pipeline (Koster and Rahmann, 2012). Briefly, raw reads were mapped by Bowtie1 (Langmead et al., 2009) and duplicate reads were removed. Only uniquely mapped reads were retained. RPKM-normalized bigwigs were generated by deepTools (Ramirez et al., 2016) and the tracks were visualized with Integrative Genomics Viewer (Broad Institute) (Robinson et al., 2011). Peaks were called using MACS1.4 (Zhang et al., 2008) with a p value of 1.0 × E-8. Chromatin state was called using ChromHMM (Ernst and Kellis, 2012) and the emission profiles were plotted by ComplexHeatmap (Gu et al., 2016). The heatmaps were generated by R package EnrichedHeatmap. ChIP-seq peaks were annotated with the nearest genes using ChIPseeker (Yu et al., 2015). Super-enhancers were identified using ROSE (Loven et al., 2013) based on H3K27ac ChIP-seq signals.

Publicly available PER2 ChIP-seq data for mouse (GEO: GSE3997) were reanalyzed by using six samples (GSM982733, GSM982734, GSM982735, GSM982736, GSM982737 and GSM982738). Another data GSM982739 was excluded because it was from a *Per2* knock-out mouse. The raw FASTQ files were aligned to mm9 genome separately for each sample using the same Snakemake pipeline. The read duplication rate was high, and the bam files after alignment were merged together. A bigwig file normalized to RPKM was derived from the merged bam file for visualization. The bigwig tracks were plotted using karyoploteR (Gel and Serra, 2017).

ChromHMM Transition

ChromHMM profiles of two *Kras*;*Kmt2d*$^{-/-}$ and two *Kras* samples were consolidated using Epilogos (https://github.com/Altius/epilogos). A pipeline was made to automate the calculation, and the scripts used to re-code the ChromHMM states can be found https://github.com/crazyhottommy/pyflow-chromForest/tree/vsurf_merge. With the Epilogos output, the chromatin state for each bin was chosen for the state that contained the greatest weights. A helper script can be also found at the above link. The output for each group was analyzed by java -mx12000M -jar ChromHMM.jar OverlapEnrichment. The matrix output from OverlapEnrichment was scaled by columns and plotted using ComplexHeatmap (Gu et al., 2016).

Glucose Uptake and Lactate Excretion Assay

Cells were seeded in triplicate in a 12-well plate. Wells containing medium but no cells were used as baseline readings. On the second day, the medium in each well (including the wells without cells) was changed with 1 ml fresh medium. After 48 hr, 600 μl medium was collected from each well. Each sample of medium was centrifuged at 3000 rpm for 3–5 min at 4°C. From each sample, 200 μl medium was transferred into a 96-well plate, and glucose and lactate levels were measured using an YSI analyzer according to the manufacturer's protocol. Each level was normalized to the cell number.

Metabolomics Experiments

All the reagents and chemicals for metabolomics experiments were described earlier (Wangler et al., 2017). For sample preparation for mass spectrometry and metabolomics analysis, metabolites were extracted from cell pellets, and mouse liver pool was used for quality control according to the previously described extraction procedures (Putluri et al., 2011, 2014). Briefly, equal number of cells from each group were used for the metabolic extraction. The metabolites were extracted with polar and non-polar solvents, and the protein content in the extracts was removed using 3 kDa Amicon ultra filters. The filtrate was dried under vacuum (Genevac EZ-2plus; Gardiner, Stone Ridge, NY). The dried extracts were re-suspended in methanol-water (50/50, vol/vol) and were subjected to liquid chromatography-mass spectrometry. Quantitative analysis using Agilent MassHunter Workstation Software was performed for review of chromatograms. Peak-area integration was accessed on the basis of the retention time. After data acquisition, the normalization of each metabolite was performed using an isotopic labeled internal standard, and the data were $\log_2$-transformed. For differential analysis, a two sample t-test was conducted. Differential metabolites were identified by adjusting the p values for multiple testing at a false discovery rate (FDR) threshold of < 0.25. The analysis was performed by the R package.

Inhibitor Experiments

Cells were seeded at a density of 1.5×10^3 cells per well in quadruplicates in 96-well plates. Plated cells for human *KMT2D*-WT LUAD cell lines (A549, H1792, H23, H1437, and H358) and *KMT2D*-mutant LUAD cell lines (H1568, DV-90, and CORL-105) were treated with a range of concentrations of various inhibitors, including 2-Deoxy-D-Glucose (2-DG; 1 to 1000 μM), POMHEX (0.05 to 2 μM), SAHA (0.1 to 20 μM) and AR-42 (1 to 500 nM), for one week. The cells were replenished with inhibitor-containing medium on alternate days. After 7 days, the cells were stained with crystal violet and quantified using Celigo. Cells treated with dimethyl sulfoxide were used as a control.

Extracellular Flux Assays Using Seahorse Analyzer

The extracellular acidification rate (ECAR) and the oxygen consumption rate (OCR) in lung cancer cell lines were measured using the Seahorse XF96e Extracellular Flux Analyzer (Agilent, USA). Cells ($1.6–2 \times 10^4$ per well) were seeded in Seahorse XF96 cell culture microplates, and the plates were incubated at 37°C under 5% CO_2. After 24-hr incubation, the media were changed to the assay medium without glucose. The ECAR (e.g., basal glycolysis and glycolytic capacity) was measured by the sequential additions of glucose (at a final concentration of 10 mM), oligomycin (1.0 μM), and 2-DG (50 mM) in the Seahorse Analyzer using the Glycolysis Stress Test Kit (Agilent, USA). The glycolysis and glycolytic capacity were calculated according to manufacturer's protocol. The OCR was assessed by the sequential additions of oligomycin (1.5 μM), Carbonyl cyanide-p-trifluoromethoxyphenylhydrazone (FCCP, 1.0–2.0 μM), and antimycin A (0.5 μM)/rotenone (1 μM) in the Seahorse Analyzer using the Cell Mito Stress Test Kit (Agilent, USA). Both ECAR and OCR were measured over a 3-min period and normalized to the protein concentrations that were determined by the Bradford assay.

Three-Dimensional Cell Culture

The three-dimensional (3D) cell culture methods were adapted from the previously described procedures (Lee et al., 2007a). In brief, a 96-well plate was coated with 6 μl of Engelbreth-Holm-Swarm tumor matrix (Matrigel, BD Biosciences) and kept on room temperature for 30 min. Cells were trypsinized and suspended in Dulbecco modified essential medium (DMEM) containing 50% Matrigel. Cells (2×10^5 per well) were seeded in the plates. Every third day, the cells were replenished with fresh DMEM containing 10% fetal bovine serum. The cells were cultured for 10–14 days.

In Vivo Inhibitor Experiments

Cells (5×10^6) in 100 μl Matrigel were subcutaneously injected in both flanks of 6- to 8-week-old athymic nu/nu mice. Eight days later, mice that had developed palpable tumors were randomly separated into two groups. One group of mice was treated with 2-DG (500 mg/kg body weight) or KA (1 mg/kg body weight) via intraperitoneal injections on alternate days for 16–20 days. Because the drug was prepared in sterile water, the other group was injected with sterile water as a vehicle control. Tumors were measured on alternate days by caliper. Tumor volumes were calculated using the ellipsoid volume formula ($1/2 \times l \times w \times h$) as previously described (Wagner et al., 2013). After 16–20 days of treatment, the mice were euthanized and tumors were collected for histologic analysis.

Stable Knockdown, Overexpression, and Rescue Experiments

For knockdown experiments, lentivirus-based, puromycin-resistant shRNAs were purchased from Sigma Chemicals (Key Resources Table). The shRNA-infected cells were selected in puromycin-containing medium (1 μg/ml). shLuc-infected cells were used as a control. For ectopic expression experiments, human *PER2* cDNA was cloned into the lentivirus vector pLenti6.3/V5-DEST (Thermo Fisher Scientific) using standard cloning methodology. Cells infected with pLenti-*PER2* were selected in blasticidin-containing medium (2 μg/ml). pLenti-GFP-infected-cells were used as controls. For doxycycline (Dox)-inducible *KMT2D* expression, *KMT2D* cDNA in pDNR221 (a kind gift from Dr. Laura Pasqualucci) was cloned into pInducer20. The expression plasmid was transfected into H1568 cells using Lipofectamine 3000. The cells were then selected in 1 mg/ml G418 for 2 weeks. *KMT2D* expression was induced by the medium containing 10 μg/ml Dox.

For rescue experiments, KMT2D-depleted LKR10 cells were seeded and 24 hr later transfected with pFLAG-CMV2 expression plasmids encoding mini-KMT2D or GFP. Of note, the mini-*KMT2D* construct was previously described as $MLL4_{\mathrm{fusion}}$ construct (1358-1572aa/4507-5537aa) (Dhar et al., 2012). As a control, shLuc-treated LKR10 cells were transfected with pFLAG-CMV2 expression plasmid encoding GFP. Two days later, these cells were harvested. Total RNAs were isolated for qRT-PCR analysis. Quantitative ChIP analysis was performed as previously described (Dhar et al., 2012).

Measurement of GAPDH and Enolase Activities

GAPDH and Enolase assays were performed according to the manufacturer's protocols (Abcam, USA). Briefly, cells (1×10^6 per well) were lysed in GAPDH and Enolase assay buffers. GAPDH and enolase assays were performed using 4–5 μg and 2 μg of lysates, respectively. Protein quantification of lysates was performed using the bicinchoninic acid (BCA) protein assay Kit (Pierce, USA). The absorbance of 450 nm at a 60 min reaction and 570 nm at a 30 min reaction was measured to calculate GAPDH and Enolase activities, respectively.

QUANTIFICATION AND STATISTICAL ANALYSIS

In all the boxplots, the bottom and the top rectangles indicate the first quartile (Q1) and third quartile (Q3), respectively. The horizontal lines in the middle signify the median (Q2), and the vertical lines that extend from the top and the bottom of the plot indicate the maximum and minimum values, respectively. The two-tailed Student's t-test was used to determine statistical difference between two boxplots as well as between certain two groups (where indicated). Survival differences were compared by the Kaplan-Meier method using the two-sided log-rank test (IBM SPSS Statistics 23). Data are presented as means ± standard error of the mean (SEM; error bars) of at least three independent experiments or three biological replicates. p values less than 0.05 were considered statistically significant. * ($p < 0.05$), ** ($p < 0.01$) and *** ($p < 0.001$) indicate statistically significant differences between two groups.

Please cite this article in press as: Alam et al., KMT2D Deficiency Impairs Super-Enhancers to Confer a Glycolytic Vulnerability in Lung Cancer, Cancer Cell (2020), https://doi.org/10.1016/j.ccell.2020.03.005

DATA AND CODE AVAILABILTY

The accession numbers for the RNA-seq and ChIP-seq data reported in this paper are GEO: GSE116658, GSE116659, GSE143498. The pipelines and code to process the RNAseq and ChIPseq data are available at https://github.com/crazyhottommy/pyflow-RNAseq, https://github.com/crazyhottommy/pyflow-ChIPseq and https://gitlab.com/tangming2005/kmt2d-lung-cancer-cell-paper-2020.